Experimental Study on Multiphase Flow in Fracture-Vug Medium using 3D Printing Technology and Visualization Techniques

Wei Yang[a], Dongxiao Zhang[b*], and Gang Lei[c]

[a] BIC-ESAT, ERE, and SKLTCS, College of Engineering, Peking University, Beijing 100871, P. R. China

[b] School of Environmental Science and Engineering, Southern University of Science and Technology, Shenzhen 518055, P. R. China

[c] CPG, King Fahd University of Petroleum and Minerals, Dhahran 31260, Saudi Arabia

* Corresponding author. E-mail address: donzhang01@gmail.com (D. Zhang).

Abstract

Strong heterogeneity and anisotropy exist in fractured-vuggy reservoirs, resulting in complex flow and relatively low oil recovery. Therefore, the mechanism of water flooding and gas injection displacement in fracture-vug medium constitutes a key issue in oil production. In this study, based on similarity criteria, physical models of fracture-vug medium are designed and constructed through 3D printing technology. Then, by combining the LED (light-emitting diode) backlight visualization method (BVM) and the particle image velocimetry (PIV) technique, experiments of multiphase flow (i.e., oil-water and gas-oil) through the printed fracture-vug medium are carried out. During the experiments, the morphological changes of the fluid interfaces are captured with BVM, and the velocity field and streamlines of the fluid in the system are determined by the PIV technique. In addition, we also investigate various factors affecting the recovery efficiency of fracture-vug medium, such as injection velocity, gravity, outlet position, and shape factors. Results show that oil recovery in fracture-vug medium varies with injection velocity (or Reynolds number), shape of the vug, and fracture-vug structure. Specifically, the distribution of remaining oil is affected by the shape of the vug. Gravity also exerts a great influence on the morphology of bubbles in the case of gas injection. The present study leads to a better understanding of multiphase flow in fracture-vug medium and a valuable experimental dataset.

1. Introduction

It is well known that carbonate reservoirs account for 60% of the world's oil reserves, in which 30% of carbonate reservoirs are fractured-vuggy reservoirs (Yao and Huang, 2017). In general, strong heterogeneity and anisotropy exist in fractured-vuggy reservoirs, with the following characteristics: (1) the reservoir types are complex and their scale range is quite wide, in which the spatial size of fractures and vugs may range from micrometers to meters (Yang, 2012); (2) fluid exchange occurs between different components (i.e., the vug, the fracture, and the matrix) in the system of multiple media (Arbogast and Brunson, 2007; Hui et al., 2015; Peng et al., 2009); (3) the connectivity and distribution of these systems are complex and difficult to conceptualize. Moreover, in fractured-vuggy reservoirs, it is challenging to find a representative elementary volume (REV), unlike in sandstone; and (4) fluid flow regimes in fracture-vug medium are a complex coupling system: there are free flows in unfilled vugs, linear flows in large fractures and Darcy flows in the micro-fractures and matrix, resulting in a complex fluid flow mechanism (Yao and Huang, 2017). In the published literature, many scholars found that the permeability of the matrix system was far less than that of the other two systems, and they suggested that fluid flow in the matrix system can be neglected (Dong et al., 2011; He et al., 2017; Hui et al., 2015; Lyu et al., 2017).

Water injection is an effective way to supplement formation energy. However, when water cut increases up to a certain value, continuous water injection may lead to reductions of the efficiency of oil production. Moreover, remaining oil can be of a significant amount after water flooding. As a typical fractured-vuggy reservoir, the Tahe oilfield (China) has been exploited by water flooding

with good oil production at early times (He et al., 2017; Lv et al., 2011). However, a series of problems occurred during water flooding (Camacho Velazquez et al., 2002; He et al., 2017; Karimaie et al., 2008; Lyu et al., 2017). For example, when the reservoir development enters the high water cut stage, most of the injected water directly flows through high permeability channels (e.g., fracture system and vug system), resulting in short production time and low oil recovery. As a result, many researchers have performed physical experiments to better understand the characteristics of the water flooding mechanism in fracture-vug medium (Ahmadi and Shadizadeh, 2013; Cruz-Hernandez et al., 2001; Dabbouk et al., 2002; Dong et al., 2011; Rezaei et al., 2013; Xie et al., 2017). Due to the complex fracture-vug structure, however, the mechanism of water flooding in fracture-vug medium remains unclear, and further research is needed to more fully elucidate the water flooding process.

As an alternative method, nitrogen injection has become one of the often used approaches for enhanced oil recovery (EOR) since the 1980s (Lyu et al., 2017; Mohsenzadeh et al., 2016). Nitrogen injection is effective if the primary purpose of the injection is pressure maintenance and/or nitrogen is injected from the top (gas-assisted gravity drainage). Numerous researchers have conducted nitrogen injection experiments, and reported that nitrogen possesses great potential in improving oil recovery in fractured-vuggy reservoirs (Hui et al., 2015; Karimaie et al., 2008). Since 2012, field-scale experiments on nitrogen injection EOR have been carried out on Tahe fractured-vuggy reservoirs, and good results were achieved (Karimaie et al., 2008; Lyu et al., 2017; Wu et al., 2011). In general, the nitrogen injection EOR works because the injected nitrogen not only maintains formation pressure, but also displaces and replaces oil under gravity. In addition, after the injected nitrogen is dissolved in the crude oil, it increases the volume of the crude oil and reduces its viscosity (Karimaie et al., 2008; Mohsenzadeh et al., 2016; Wu et al., 2011; Yao and Huang, 2017). However, nitrogen injection may not always be effective, in that injected nitrogen can end up with earlier breakthrough and severe gravity override. In addition, unlike CO_2, it is quite difficult to achieve first/multi-contact miscible displacement. Furthermore, under real Tahe reservoir formation conditions (buried depth is below 5000 m, original formation pressure is approximately 60 MPa, formation temperature is approximately 125 °C), the nitrogen phase state changes greatly, which causes high uncertainty in nitrogen injection evaluation. Relevant work focusing in detail on the analysis of the mechanisms of nitrogen injection in fractured-vug medium is scarce. Motivated by this, in this paper, we investigate the mechanisms of water flooding and gas injection in fracture-vug medium in a detailed manner.

To elucidate the mechanisms of multiphase flow in facture-vug medium, many methods have been proposed to visualize fluid flow through fracture-vug micromodels produced by etching two- and three-dimensional fracture-vug network structures into different materials, such as silicon (Willingham et al., 2008; Zhang et al., 2010), glass (Ferer et al., 2004), poly-dimethyl-siloxane (PDMS) (Cottin et al., 2010; Wu et al., 2012), and polyester resin (Chang et al., 2009; Cheng et al., 2004; Lenormand et al., 1988). With cameras or fluorescent microscopy, fluid flow behavior through fracture-vug micromodels can be observed. Moreover, subsequent quantitative evaluation of fluid saturation and interfacial area can assist us to better understand multiphase flow processes at the microscopic level (Willingham et al., 2008; Zhang et al., 2010; Zhang et al., 2011). With added tracer particles or fluorescent particles, the velocity field could also be measured by the PIV method. It should be noted that, even though traditional visualization materials have been successfully applied to experimental models, a number of disadvantages also exist. For instance, the etching models often need to be spliced and glued together (Chen et al., 2016), and the sealing properties of the model are greatly affected by the processing technology, resulting in limited experimental pressure. In addition, micromodels processed by traditional visual materials possess great limitations regarding high temperature, specific pH, hardness, and wettability. The physical dimension of the model is also relatively narrow and limited to a certain size.

In this work, we improve the wide applicability of the micromodel by utilizing 3D printing technology, which is a method of rapid prototyping and mass production by sequential layer-by-layer printing (Ishutov et al., 2015; Lifton, 2016). In general, 3D printing can produce integrated molding to ensure that the model is sealed and has a certain capacity to bear pressure. The

3D printing model can also account for numerous factors, such as wettability, surface tension, surface structure, pore-filling, multi-scale, etc. Most importantly, the 3D printing model can achieve physical model repeatability and controllability, and meet various experimental requirements. The actual fracture-vug structure is complex, and we select most crucial parameters through a similarity criterion (i.e., the similarity of dynamics, movement, and geometric features) to characterize flow in fracture-vug medium. Firstly, 3D printing technology is employed to produce a fracture-vug medium physical model that is visible and exhibits integrated molding (pressure-resistant). Then, by combining the BVM and PIV methods, we perform experimental tests on the printed fracture-vug physical model to investigate multiphase flow behaviors in fracture-vug medium.

The remainder of this paper proceeds as follows. The experimental work is presented in the following section. Based on similarity criteria (i.e., the similarity of dynamics, movement, and geometric features) and field-scale production data, laboratory-scale parameters will be determined through dimensional analysis. We choose appropriate 3D printing technology to establish a conceptual fracture-vug medium which is both highly transparent and possesses a certain capacity to bear pressure. In addition, based on the printed visual physical model, we conduct a series of water flooding and gas injection experiments. The results are then analyzed, followed by a discussion of the results. Finally, the study is summarized with the main findings.

2. Methods

2.1 Similarity criteria

In order to make the experimental results more robust and generalizable, flow characteristics at the laboratory-scale should be similar to those at the field-scale. Based on dimensional analysis, seven similarity criteria that could reflect the main characteristics of fractured-vuggy reservoirs are determined (shown in Table 1). For example, to ensure geometric similarity, the ratio of wellbore radius to reservoir thickness in the physical model should be equal to that in the actual fractured-vuggy reservoir model (Hou et al., 2014). Concerning movement similarity, because fluid flow appears as free flow in the vug and linear flow in the large-scale fracture, the similarity design of the physical model should satisfy the Reynolds number that achieves similar characteristics of fluid flow. In general, it is difficult to fulfill all similar criteria simultaneously, and thus we need to focus on the main similarity criteria. Firstly, the Reynolds number similarity criterion should be satisfied, as shown in Eq. (1). The parameters in the physical model should also be adjusted to meet the ratio of pressure to gravity, as shown in Eq. (2). In addition, other important parameters, such as coordination number (the number of fractures connected by the reservoir (vug)), filling degree, and number of connected fractures should be employed as characteristic parameters in fracture-vug medium. To simplify the model, in this paper, the coordination number is selected as 1 (one fracture connecting a vug), and the filling degree is 0 (the filling condition is not considered). For instance, in order to achieve motion similarity, the flow parameters in the model should satisfy the Reynolds number of the oilfield (Hou et al., 2014). Eq. (1) is obtained as follows:

$$\mathrm{Re} = \frac{\mu}{\rho u L} \Rightarrow u_{\mathrm{e}} = \frac{\mu_{\mathrm{e}} \rho L}{\rho_{\mathrm{e}} \mu L_{\mathrm{e}}} u \Rightarrow u_{\mathrm{e}} \in \left[0.002 - 1.67\,\mathrm{m/s}\right] \tag{1}$$

where u, ρ, and μ are the fluid velocity, fluid density, and fluid viscosity coefficient, respectively; L is the characteristic length (e.g., reservoir thickness); and subscript e represents the parameters in the physical model. Based on Eq. (1) and Table 2, velocity in the physical model should range from 0.002 m/s to 1.67 m/s. Thus, during the tests, fluid injection should be constrained to ensure that the velocity is within this reference range. Moreover, to satisfy the similarity of dynamics, Eq. (2) is attained as follows:

$$\chi = \frac{\Delta p}{\rho g L} \Rightarrow \Delta p_e = \frac{\rho_e g L_e}{\rho g L} \Delta p \Rightarrow \Delta p_e \in [2.26\text{-}45.3\text{kPa}] \quad (2)$$

where χ is the ratio of pressure to gravity; g is the gravity; and Δp is the pressure difference. Eq. (2) shows that the pressure difference in the physical model ranges from 2.26 kPa to 45.3 kPa. According to the similarity criteria, other parameters used in the physical model are determined (shown in Tables 2 and 4). Specifically, nitrogen is utilized as the gas phase, ultra-pure water serves as the water phase, and Silicone oil DC 200 is used as the oil phase.

2.2 Parameters of the physical model

The following assumptions are made prior to introducing the parameters of the physical model:

- Compared to the permeability of the fracture or the vug, the permeability of the matrix system can be ignored. As a result, the contribution of the matrix system to fluid flow in fracture-vug medium can also be ignored.
- The dissolution of nitrogen in water and oil is negligible. Oil-gas-water is in an immiscible state, and a clear interface exists between them.
- In this paper, we take larger vugs of the Tahe oilfield as an example. These larger vugs are only connected to smaller number of larger scale fractures. Sometimes, a larger vug is only connected to a larger scale fracture. Therefore, to simplify the model, the coordination number is selected as 1 (one fracture connecting a vug), and the filling degree is 0 (the filling condition is not considered).

Based on similarity criteria, we design two typical fracture-vug models (Fig. 1), in which the fracture dip angle is represented by ω. Fracture dip angle $\omega \approx 0$ means that the fracture is close to the horizonal state in the formation, and fracture dip angle $\omega \approx \pi/2$ means that the fracture is close to the vertical state in the formation. Schematic diagrams of the fracture-vug model are shown in Fig. 2. The physical parameters of the fracture-vug model are presented in Table 4. The range of fracture aperture is 0.5-2 mm, the diameter of the vug is 50 mm, the ratio of the vug diameter to the fracture aperture is approximately D_v/W_f=25-100, and the effective thickness of the model is 2 mm. The physical model has a size of 100 mm×100 mm×12 mm. Fig. 3 shows the actual physical fracture-vug model by 3D printing that is highly transparent and has a certain pressure-bearing capacity.

2.3 Construction of the physical model

In this study, we employed the Objet350 Connex3 3D printer (shown in Fig. 4a) to produce the fracture-vug model. The device has a print resolution of up to 600×600×1600 dpi with a dot accuracy of 16 μm /30 μm (high-quality printing has an accuracy of 16 μm, and high-speed printing has an accuracy of 30 μm), and a molding thickness of 16 μm. The maximum size of the printing model is 340×340×200 mm^3. The printer can utilize 16 different types of basic photopolymer materials to generate hundreds of composite digital materials by specific mixing ratios, thus allowing the mechanical properties of composite materials to match the natural sample. This printer also facilitates the production of a multi-component material model. The Objet350 Connex3 3D printer offers the major advantages of high precision and automation, and ease to create complex 3D models. The printing mechanism of the Objet350 Connex3 3D printer is PolyJet technology (shown in Fig. 4b). PolyJet is a powerful 3D printing technology that produces smooth, accurate parts, prototypes, and tooling. With microscopic layer resolution and accuracy down to 0.1 mm, it can produce thin walls and complex geometries using the widest range of materials available with any technology. We adopted the transparent photopolymer Vero Clear to produce the matrix, and the lite-type latticed supporting material Fullcure 706 was adopted to form the fractures and vugs (Ju et al., 2014). Fullcure 706 is a water-soluble material, which can be rinsed with a 2% wt NaOH + 1% wt Na_2SiO_3 aqueous solution for a long time to form fractures and vugs (shown in Fig. 3).

The model is soaked in aqueous solution for a long time (about a few days or more), resulting in a change in surface wettability (as shown in Fig. 5a), which becomes water-wet. In the actual formation, the rock is mainly oil-wet, so it is necessary to modify the wettability of the model. The transparent superhydrophobic coating SM-101S is selected for modification. The modified oil-gas-water contact angle of the model is presented in Fig. 5b, in which gray is the water phase, transparent is the oil phase, the circle is the gas phase, and the contact angle is visible: oil-wet>water-wet>gas-wet.

2.4 Experimental equipment

A streamline diagram of the fracture-vug system multiphase flow visualization platform is shown in Figs. 6 and 7. The experimental setup was composed of three ISCO (one single-cylinder 65D and two dual-cylinder 100DX) pumps for high-pressure injection fluid (or three creepage (LSP01-1BH) pumps for low-pressure injection fluid), an intermediate piston container (16 MPa, 200 ml), a PCO.dimax CS1 high-speed camera (3086 FPS @ 1296 x 1024), an LED surface light source, a continuous laser (wavelength 532 nm, 25 W), a model holder, a back pressure system (1.6 MPa, 0.1FS %), and Keller differential pressure transducers. The model holder could realize 360° rotation for the two-dimensional model and 0.1 mm precise movement for the three-dimensional model. Firstly, oil, gas, and water are filled into the corresponding intermediate containers, respectively, and the pumps push the bottom of the container, and the middle pistons push fluid into the model. The back pressure is sited at the outlet of the model, and the fluid flow process is recorded by a high-speed camera in the visualization model. When we study the characteristics of the export fluid, we can increase electronic balance (0.01 g) or gas flowmeter (0.5~50 ml/min).

2.5 Experimental procedure

Based on the experimental system and equipment (Figs. 6 and 7), five parts, i.e., the injection system, the control system, the imaging system, the back pressure system and the data acquisition system, water flooding and gas injection experiments of the fracture-vug model are performed. Fig. 8 presents the specific experimental procedure.

- **3D printing physical model.** The physical model is transparent and is produced by 3D printing. The physical model assistance system comprises two parts: the model holder system and the light source. For the model holder part, we choose an aluminum alloy custom structure to achieve stability of the physical model, and can realize the rotation of the model at different angles and study the flow state at different angles. Concerning the light source part, different light sources are chosen for different experiments. First, we choose an LED surface light source to focus on the fluid flow state, gas characteristics, and sweep volume by LED BVM. Then, we choose 532 green lasers to focus on oil-water-gas fluid velocity characteristics, fluid separation, and fusion through the PIV method.
- **Constant flow injection system**. The experiment is carried out at room temperature with a back pressure of 120 KPa. Based on the 3D printing physical model, a constant pressure gas is saturated to check for gas leakage. If not, we allow a vacuum for 12 h, and then saturate in oil for 2 h. We then perform the gas injection experiments (or water flooding experiments). Water injection (or gas injection) is next carried out when no oil is displaced from the outlet (shown in Fig. 8). The multiphase flow experiments in the fracture-vug model are performed based on the following aspects: different injection velocities, different injection fluids (oil, gas, water), different gravity states (horizontal or vertical section of the model), and different injection positions.
- **Control system.** In the experiment, the contact area with the physical model is controlled by a pneumatic automatic control in order to avoid human interference with observation and recording.

- **Data acquisition and processing system.** The data in the experiment mainly include injection flow rate (pressure), dynamic image of physical model fluid, and pressure difference between the model. The injection flow rate pressure is derived from the injection pump record; the flow image is obtained from the high-speed camera imaging data volume; and the pressure difference between the model is derived from the differential pressure sensor. Data processing is mainly performed with image processing software, such as ImageJ and MATLAB. PIV calculations are derived from open source PIV code calculation.

2.6 Experimental technology

Due to the different aspects of fluid flow in fracture-vug medium, in this paper, we choose two different technologies, i.e., BVM (as shown in Fig. 9) and PIV (as shown in Fig. 10). The following are briefly introduced for the two methods, respectively.

LED BVM. The experimental principle of LED BVM is presented in Fig. 9. Based on the two-dimensional or quasi-three-dimensional visualization model (radial depth is far less than plane size), the LED surface light source is arranged on one side, and image recording equipment, such as the high-speed camera, is distributed in parallel on the other side. In the process of recording experiments, quantitative research using the image processing program is carried out, and the problems of fluid flow pattern, multiphase interface change, gas characteristics, sweep volume, and wettability turn are investigated. BVM does not require tracer particles, unlike PIV, with an emphasis on studying interphase interactions. Since the refraction of light at the interface is negligible, the experiment is easier to operate.

PIV method. The experimental principle of PIV (shown in Fig. 10) is to add tracer particles (such as fluorescent particles) into the fluid, which can reflect characteristics of the fluid flow. The particles need to follow the flow of the fluid. Under general conditions, the BBO equation (Basset, 1961) could be utilized to describe the dynamic properties of the particle following the fluid (Eq. 3). The simplified equation is as follows:

$$\begin{aligned} u_p &= u(1-e^{-kt}) = u(1-e^{-t/T}) \\ T &= 1/k = \rho_p d_p^2 / 18\mu \end{aligned} \tag{3}$$

where u_p is the velocity of particle; u is the velocity of fluid; t is the time; ρ_p is the density of particle; d_p is the diameter of particle; T is the delay time; and k is the reciprocal of T. In general, the smaller is the T, the better is the particle followability. However, the particle diameter is too small to satisfy the reflected light intensity. In this paper, we select melamine formaldehyde resin (aqueous dispersion) as the fluorescent particles. The composition of the fluorescent material is Rhodamine B, which is orange fluorescence. The particle density is 1.51 g/cm^3, and the average particle diameter is 7 μm. The excitation wavelength of the particles is 550 nm, and the emission wavelength is 584 nm. We choose a 532 green laser surface light source.

Unlike BVM, the laser is placed on the same side as the high-speed camera, which has a filter in front of the lens and is perpendicular to the model. The laser has a certain angle α to the physical model for exciting fluorescent particles, as shown in Fig. 10(d). A high wave long light is emitted by the laser excited by a certain wavelength (532 nm), and the image recording device is configured with a filter to record two continuous particle images of a certain time interval. The displacement of a small group of particles in a certain area is calculated, and the local velocity is obtained by dividing the displacement by a time interval. In the whole image, all of the cell processing occurs in the velocity distribution of the whole field. The computing methods are mainly autocorrelation and cross-correlation methods for PIV. The autocorrelation method is applied to the case of particle images used for two successive exposures in the same pair of images; whereas, the cross-correlation method is applied in the case of two exposure particle images recorded on two successive images. In this paper, we choose the latter, and the following are the specific steps: (1) the particle image is segmented by the mesh region, and each mesh region represents a point in the flow field; (2) the particle images of each grid area are sequentially calculated; and (3) in the case in which the particle

group itself has less influence, the magnitude and direction of the displacement of the particle group in the corresponding mesh region are obtained.

3. Results and discussion

Based on the physical model, experimental platform and experimental technology introduced in the previous section, a series of experiments based on BVM and PIV methods were carried out. Among them, the BVM experiments were divided into two parts: fracture dip angle $\omega \approx 0$ (horizontal fracture) and fracture dip angle $\omega \approx \pi/2$ (vertical fracture); and PIV experiments had three parts: single oil-phase flow, oil-water two-phase flow, and oil-gas two-phase flow. In the experiments, sweep efficiency was represented by Se, pore volume was represented by PV, and injection velocity was represented by a logarithm of the capillary number (Ca), i.e., LCN (Eq. 4):

$$\log(Ca) = \log(\frac{\mu u}{\sigma}) \tag{4}$$

where μ is fluid viscosity; and σ is interfacial tension.

3.1 Experiment based on BVM

3.1.1 Fracture dip angle $\omega \approx 0$

The left end is the injection well, and the right end is the production well, i.e., the flow direction is from left to right. In Figs. 11-16, oil, water, and gas are marked in red, blue, and green, respectively. Figs. 12, 14, and 16 show sweep efficiency statistics of gas-oil or water-oil versus injection velocity at different injection pore volumes. There is a certain deviation in the sweep efficiency of the same PV number for different injection velocities during non-steady state, but at steady state, the final sweep efficiency is the object of analysis. The following experiments are also based on this principle.

Case 1: Horizontal gas injection experiments

Comparing Figs. 11(a_i-d_i) and (A_i-D_i), the experiment results of the spherical model and the square model share many similar features. Initially, the gas flow appears as a piston displacement in the inlet fracture. After the gas phase enters the vug, the gas bubble gradually becomes bigger until the gas breakthrough. The entire process constitutes a piston displacement. At the steady state, the gas distribution is symmetric about the horizontal midline. Different injection velocities of gas phase have different effects on the displacement process and results. In the experiment, a lower LCN (i.e., -6) would decrease gas pressure, and thus the continuous phase oil easily “breaks” the gas phase flow, resulting in the formation of a number of continuous bubbles. Consequently, gas can fully spread in the vug to enhance the recovery factor. As the LCN increases (i.e., -5), the gas pressure is also large, and it is not easily broken by the oil during the gas into the vug, and the gas flow is a continuous flow. However, when the LCN is large, the shape of the gas is greatly affected by the pressure difference and the viscous force, and the smoothness of the shape of the gas boundary is decreased. Moreover, as the LCN increases (i.e., -4), the sweep efficiency of gas injection decreases, and the recovery factor decreases (Fig. 12).

Although the experimental results of the two models possess numerous similarities, some differences exist in the experimental results. Specifically, the four corners of the square model always have no fluctuation of gas phase flow. When the LCN is relatively large (LCN=-5, -4), the recovery factor of the square model is lower than that of the spherical model. However, when the LCN is small (LCN=-6), the recovery factor of the square model is approximately 6.4% higher than

that of the spherical model (Fig. 12). In the equal-area vug, the position (line or point) away from the horizontal midline in the vug of the square model is smaller than that of the spherical model. When the injection velocity is small, the gas phase is more likely to reach the region away from the horizontal midline in the square model. In addition, the displacement efficiency of the square model is higher than the displacement efficiency of the spherical model. The specific reason for this will be verified in the next PIV experiments.

Case 2: Vertical gas injection experiments

In the spherical model (Fig. 13(a_i-e_i)) and the square model (Fig. 13(A_i-E_i)), the flow of the gas phase in the inlet fracture appears as a piston displacement, but gravity makes the interface no longer symmetric about the horizontal midline at the displacement front. After the gas enters the vug, the gas phase becomes discontinuous due to gravity, forming equal diameter bubbles and rising rapidly along the wall to the top of the vug. As the bubbles accumulate at the top, the bubbles overcome the interfacial tension and gradually merge into larger bubbles, resulting in oil displacement. When the oil-gas interface moves from the top to the horizontal midline, after the gas phase flows out of the fracture, the oil recovery factor no longer changes.

Comparing the results of the two models, the bubbles rise along the wall to the top in the spherical model during low injection velocity. As the velocity of the gas injection increases, the bubbles flow upward far away from the wall in the spherical model, which is the same as in the square model. This is due to that the trajectory of the bubble depends on velocity in the horizontal direction and gravity in the vertical direction. The diameter of the bubble is related to the width of the fracture and the injection velocity, regardless of the shape of the vug. Overall, the larger is the fracture width and the higher is the gas injection velocity, the larger is the bubble size.

Comparing different LCNs, the fusion time of bubbles varies with the injection velocity. Specifically, when the LCN is small (i.e., -6), the gas-oil interface is little affected by gravity in the inlet fracture, and the gas enters the vug with small bubble diameter and smooth shapes. In addition, the fusion time of bubbles is sufficient. The oil-gas interface pushes downwards horizontally in the vug, and when the interface reaches the outlet fracture, the gas flows out smoothly. However, when the LCN is large (i.e., -4), the gas-oil interface is significantly affected by gravity in the inlet fracture, and the gas enters the vug with a larger bubble diameter. The fusion time of bubbles is insufficient and the pressure at the top is large, resulting in an extrusion deformation of the bubbles. When the gas-oil interface is close to the outlet fracture, the gas exhibits obvious turbulence and releases instantaneously. Consequently, more oil film exists between bubbles in the displacement process, and thus the injected PV number must be increased to clean the oil film. With the increase of injection velocity, the displacement efficiency decreases slightly (Fig. 14).

Compared with case 1, for the vertical model setup, gravity plays an obvious role, and the gas phase swept area is mainly the upper part of the horizontal midline. For the horizontal model setup, there is no gravity effect, and the swept areas are mainly distributed in the area around the symmetry axis of the horizontal midline.

Case 3: Vertical water injection experiments

In the square model and the spherical model, the injection velocity increases from left to right, as shown in Fig. 15, and the water phase gradually changes from separation flow to continuous flow. As the LCN is low (i.e., -4.3, -3.3), after the water phase enters into the vug, water flows downward due to gravity, and the water phase is broken to form water droplets. Furthermore, the diameter of the droplets becomes larger as the LCN becomes larger. The droplets are fused together at the bottom of the vug by overcoming the interfacial tension. As the water phase continues to be injected, the oil-water interface slowly rises to the outlet fracture of the model. After water breakthrough, the recovery rate is maximized. Because the oil-water density difference is much smaller than the

oil-gas density difference, the gravity differentiation of the oil-water phase is not as obvious as that of the oil-gas phase. Therefore, the oil-water interface crossed the horizontal midline in the vug, resulting in displacement of the oil phase above the horizontal midline. As the LCN is relatively large (i.e., -2.3), the water phase forms a continuous flow, as shown in the spherical model (Fig. 15). The displacement efficiency gradually decreases as the velocity increases (shown in Fig. 16). In addition, with the increase of injection velocity, there is residual oil at the inlet region of the vug, which is the lower part of the horizontal midline. Because the increase of velocity leads to a larger velocity at the inlet fracture and a smaller velocity field at the lower part of the inlet region, a residual oil phase results. The specific reason for this will be confirmed in the next PIV experiments.

3.1.2 Fracture dip angle $\omega \approx \pi/2$

This part is in the experiment of the vertical model setup. There are two cases of flow direction: (1) "injection from the top", in which the top end is the injection well and the bottom end is the production well, i.e., the flow direction is from top to bottom; and (2) "injection from the bottom", in which the bottom end is the injection well and the top end is the production well, i.e., the flow direction is from bottom to top. This is the same as in the cases of fracture dip angle $\omega \approx 0$, as shown in Figs. 17-22, in which red is oil, green is gas, and blue is water. Figs. 18, 20, and 22 show sweep efficiency statistics of gas-oil or water-oil experiments with different injection velocities at different injection pore volumes. There is a certain deviation in the sweep efficiency of the same PV number for different injection velocities during non-steady state, but at steady state, the final sweep efficiency is the object of analysis. The following experiments are also based on this principle.

Case 4: Vertical gas injection from the top

The experimental results at different gas injection velocities, in which gas is injected from the top, are shown in Fig. 17. The gas phase occupies the top of the vug, and the oil-gas interface smoothly moves down, exhibiting a piston flow, and the displacement front is symmetrical with respect to the vertical midline. Comparing the LCN, the larger is the LCN, the easier it is to form the remaining oil at the outlet of the vug (Fig. 17). Because the differential pressure between the inlet and outlet is larger and the velocity of gas flow at the outlet is faster, gas coning appears. Therefore, the remaining oil at the bottom of the vug has not been completely displaced. Comparing the results of the different models, the oil phase in the spherical model is more easily displaced than that of the square model (Fig. 18). In the spherical model, the oil phase in the vug can be completely displaced by increasing the gas injection PV number. However, even though the gas injection PV number is increased, there is still remaining oil at the bottom of the vug in the square model. Moreover, the outlet of the spherical model is convergent, while the outlet of the square model suddenly becomes smaller, resulting in slightly higher recovery efficiency in the spherical model than in the square model.

Case 5: Vertical gas injection from the bottom.

Different from case 4, the experimental results at different gas injection velocities, in which the gas is injected from the bottom, are shown in Fig. 19. Due to the density difference between oil and gas, the gas phase enters the vug, forms a series of bubbles, and quickly rises to the top outlet. The displacement front is symmetrical with respect to the vertical midline. The diameter of the bubble varies with the LCN. In general, the larger is the LCN, the larger is the bubble diameter. As the LCN is small (i.e., -5), the bubbles enter the inlet of the vug, and then flow out of the vug in sequence,

which constitutes a continuous and stable bubble flow. As a result, gas-oil displacement efficiency is extremely low. However, as the LCN is large (i.e., -3.48), the bubble quickly enters the vug. Because the differential pressure between the inlet and outlet is larger and the bubble diameter is larger, the bubble cannot directly flow out, and thus the bubble is squeezed and deformed. Finally, the subsequent bubbles accumulate in a large amount, causing more bubbles to be deformed closer to the top of the vug. As the bubbles gather at the top, the oil phase of the top of the vug is displaced, and the oil recovery factor is greatly improved (Fig. 20). It can be predicted that when the LCN is increased, the oil recovery rate is higher at the same injection PV number. This is the opposite result of gas injection from the top (case 4), i.e., during gas injection from the bottom, the displacement efficiency in the square model is obviously more efficient than that in the spherical model at the same injection velocity (Fig. 20). At this point, the outlet of the vug in the square model suddenly becomes smaller, which can prevent more bubbles from flowing out quickly, thus improving displacement efficiency. Nevertheless, comparing the displacement results of gas injection from the top (Fig. 18) to those from the bottom (Fig. 20), as the gas phase is injected from the top, the displacement efficiency is more than 90%; whereas, as the gas phase is injected from the bottom, the displacement efficiency is lower than 30%. In actual production, optimal gas injection is firstly considered from the top to achieve superior recovery.

Case 6: Vertical water injection from the bottom and the top

The experimental results at different water injection directions in the square model and the spherical model with LCN= -3.3 are shown in Fig. 21. The displacement front is symmetrical with respect to the vertical midline. In the experiment of water injection from the bottom, the water flow appears as a continuous flow, and the oil-water interface rises steadily. After the water breaks through the outlet fracture, the oil recovery rate is maximized. Compared with different models, in the square model, there is residual oil that is symmetric about the vertical midline in all four corners, in which the top two corners have more oil remaining. However, in the spherical model, very little remaining oil exists at the top of the vug after water flooding. The displacement efficiency of the spherical model is 7.82% higher than that of the square model (Fig. 22). In the experiment of water injection from the top, the water flow presents a segmented flow. After the water phase enters the vug, it forms several large water droplets, which flow out of the vug in turn. The displacement process is similar to gas injection from the bottom (Fig. 19), but the density difference of oil-water is smaller than that of oil-gas, so that the diameter of the droplet is larger than that of the bubble. Comparing the different flow directions, the displacement efficiency of water injection from the bottom is much greater than that from the top. Under the same conditions, the displacement efficiency of the spherical model is higher than that of the square model (Fig. 22).

3.2 Experiment based on PIV

Through the results of BVM experiments, the displacement efficiency, the spreading law, and the interface morphology of the water or gas injection in the fracture-vug system have been investigated in detail. However, the velocity field of fluid flow remains unclear. In this part, a series of PIV experimental results are presented. The PIV experiments selected fracture dip angle $\omega \approx 0$, as in the conditions presented in section 3.1. The left end is the injection well, and the right end is the production well, i.e., the flow direction is from left to right. The PIV experiments have three parts: (1) single oil-phase flow; (2) oil-water two-phase flow; and (3) oil-gas two-phase flow. The flow mechanism of the fracture-vug system could be better elucidated by PIV experiments.

Case 7: Single oil-phase flow

By comparing the results of the entire area FOV of the model (as shown in Fig. 23 (a_1-d_1) and Fig.

24 (a_1-d_1)), the following characteristics can be identified. Firstly, as the LCN is small (i.e., -6.38, -5.38), the velocity field in the vug is relatively "homogeneous" and symmetrically distributed with respect to the horizontal midline. As the LCN is large (i.e., -3.48), the velocity near the horizontal midline is relatively larger, while the velocity away from the horizontal midline is gradually decreasing, but it is still symmetrically distributed about the horizontal midline. The inlet velocity of the swept region area exhibits a large arc shape effect, which assists the oil phase to spread. However, the outlet velocity of the swept region area is small, exhibiting a sharp-angle shape, which is expressed as the coning phenomenon. Regarding the asymmetry of the vertical midline, it is found that as the LCN increases, the ripple area of the flow field becomes smaller, and it is difficult to be fluctuated away from the horizontal midline region, which is termed "oil channeling". This is the reason why, for a horizontal setup, as the LCN increases, the swept volume is reduced, and the recovery factor is lowered.

By comparing the results of the inlet area FOV of the model (as shown in Fig. 23(a_2-d_2) and Fig. 24(a_2-d_2)), the velocity profile in the fracture is obvious, exhibiting a parallel flow velocity profile. It has a parabolic shape, in which the velocity in the area near the wall surface is close to zero, and the midline velocity is the largest. As the LCN is small (i.e., -6.38, -5.38), the velocity of the fracture to the vug area decreases rapidly. As the LCN is large (i.e., -4.38), the velocity of the fracture to the vug area decreases slowly. As the LCN increases to -3.48, a vortex exists at the interface between the fracture and the vug. The performance is not obvious, as shown in the enlarged view (Fig. 25). However, by comparing the results of the outlet area FOV (as shown in Fig. 23(a_3-d_3) and Fig. 24(a_3-d_3)), as the LCN increases, the distribution of the velocity field of the fracture-vug outlet area does not change substantially, except that the value changes.

Some differences are observed in the distribution of the velocity field between the two models. Firstly, compared with the entire area FOV, when the LCN is small (Fig. 24(a_1, b_1)), the velocity field in the four corners of the square model is not much different from other positions. However, as the LCN increases (Fig. 24(d_1))), the velocity field of the four corners of the square model is relatively smaller than other positions, resulting in the four corners being unable to "update". This is the reason why the recovery efficiency is larger when the injection velocity is small. Under equal volume of the model, the farthest boundary of the square model is closer to the horizontal midline than that of the spherical model. Therefore, at an LCN of -6, the recovery efficiency of the square model is 6.5% higher than that of the spherical model (Fig. 12). Compared with the inlet FOV area, the vortex (Fig. 24(d_2)) is easier to occur in the square model, because the vertical structure of the fracture-vug provides sufficient space for forming and developing the vortex. Under the same conditions, compared with Fig. 25(a, b), the vortex in the inlet area of the square model is easier to form and more complete.

Case 8: Oil-water two-phase flow

Fig. 26 shows the oil-water velocity field when the LCN is -2.08 in horizontal water flooding. It can be seen that the velocity at the oil-water interface is larger during the displacement process. In the process of displacement in the aqueous phase, however, the velocity field is not fully depicted. There are two main reasons for this: (1) a sudden change in pressure at the beginning of water flooding results in a decrease in the followability of the particles; and (2) water and oil have different refractive indices for lasers, but these can be reduced by adjusting the light intensity. After water breakthrough, a complete aqueous phase velocity field can be obtained (Fig. 26 (c)). Moreover, there are several vortices in the aqueous phase velocity field, while the oil phase velocity field is almost zero. As the water phase continues to be injected, the remaining oil cannot be displaced.

Fig. 27(a-d) shows four different moments during the vertical water flooding process in the spherical model. The velocity at the oil-water interface is continuous. When the water phase reaches the bottom of the vug, the direction of velocity changes at the oil-water interface, the interface velocity is displaced upwards at the lower part, and the interface velocity is downward at the inlet. Consequently, the water phase quickly fills the bottom of the vug. After water displaces the oil

phase at the bottom of the vug, the oil-water interface is displaced upwards, and the oil is rapidly displaced over the horizontal midline. When the water phase breaks through, the oil phase is balanced, and then no oil is displaced. At this time, the oil-water two-phase velocity field is relatively independent. If the water injection velocity increases, the oil phase velocity field is close to zero, and the distribution area of the water phase velocity field gradually shrinks toward the horizontal midline (Fig. 27(e)). As the injection velocity reaches LCN=-2.08 (Fig. 27(f)), the velocity field of the water phase is the largest in the horizontal midline area. Moreover, there is a reverse water velocity field in the lower horizontal line at the outlet end of the vug (Fig. 27(f) (the green dotted region)). It can be predicted that when the water injection velocity is larger, the oil phase above the horizontal center line may fluctuate, which will increase recovery efficiency. However, when the injected velocity is too large, the cost is too high in actual production.

The results of the PIV experiment in the spherical model (Fig. 27) were verified in the square model (Fig. 28). In the square model, since the fracture is connected with the $\pi/2$ of the vug, when water enters vug, water flow is easily segmented by gravity to form water droplets (Fig. 28(a)). When water droplets reach the bottom of the vug, droplets move toward the outlet direction, but the direction of velocity at the oil-water interface is obliquely downward, in a clockwise direction, and the water droplets are rotated to drive the oil phase. In Fig. 28(b, c), gas is introduced into the model during the water displacement process, and the gas has an overall fluctuation to the oil phase velocity field during the gas-leaching process. Thus, water and gas synergistically displace oil. Finally, oil below the horizontal midline is replaced by water, and oil above the horizontal midline is replaced by gas. If we continue to increase the gas injection, we can completely displace the remaining oil in the vug. However, as the water injection velocity increases, the sweeping area shrinks, and the remaining oil still exists.

Case 9: Oil-gas two-phase flow

For a horizontal setup, the oil phase velocity field of gas injection (Fig. 29) is similar to the oil phase velocity field for water flooding (Fig. 26). The oil-gas interface has a stronger reflection of the laser, and thus the oil-gas interface is more obvious than the oil-water interface. Since there are no fluorescent particles in the gas, the velocity field in the gas phase cannot be measured, but the oil-gas interface can reflect the gas displacement velocity. Comparing Fig. 29(b, c, d), as the gas injection velocity is small, the gas phase is easily broken after entering the vug due to gravity. At this point, we can examine the change of oil phase velocity field in the vug during bubble fusion. It is found that gas phase continuity is enhanced as gas injection velocity is increased.

Fig. 30 shows the oil-gas velocity field at different gas injection velocities in inlet FOV in the spherical model during vertical gas flooding. As the gas injection velocity increases, the diameter of the bubble becomes larger (such as Fig. 30(d_1-d_3)) (the size of the bubble mainly depends on the width of the fracture and the injection velocity). In addition, the oil phase velocity field gradually becomes unbalanced, which shows that the velocity field of the inlet area and outlet area are relatively larger, and the velocity fields are relatively small in other regions (such as Fig. 30(e_i-f_i)). When gas is broken by gravity, the oil in the vug flows back into the inlet fracture, causing a large vortex to form in the inlet region of the fracture-vug model, and the bubble rises along the wall surface. When the gas reaches the top of the vug, the downward displacement velocity of the oil-gas interface increases, which leads to greater oil phase velocity at the outlet. The PIV experiment results of the square model are the same as those of the spherical model. The difference is that the oil in the vug will return to the fracture when the gas is broken, causing a vortex to form in the inlet region of the model, but the bubble does not rotate along the wall.

3.3 Sensitivity analysis of multiphase flow in fracture-vug medium

Effect of injection velocity. Summarizing the above experimental results, we could determine

the change of Se with the LCN under different conditions (Table 5). For a horizontal setup, the smaller is the LCN, the smaller is the differential pressure, and the more that gas or water could displace oil away from the horizontal midline region, resulting in greater sweep efficiency. In the vertical setup, as fracture dip angle $\omega \approx 0$, the density difference of gas-oil is large, and gravity is the main effect after gas injection. Within a certain range of LCN, displacement efficiency does not change substantially. However, the water-oil density difference is small. When the LCN is small, although gravity is the main effect, because the pressure difference is small and interfacial tension exerts an influence, water could drive some oil near the horizontal midline; whereas, when the LCN is larger, the pressure difference is higher. Moreover, the water phase velocity field shrinks toward the horizontal midline, so that the oil displacement in the horizontal midline portion leads to a decrease in displacement efficiency. As fracture dip angle $\omega \approx \pi/2$, if gas is injected from the top (or water is injected from the bottom), the gas (water) appears as a piston flow. When the LCN is small, the displacement efficiency exceeds 95%. When the LCN is larger, the gas (water) exhibits a coning phenomenon at the outlet fracture, and the displacement efficiency is decreased. If gas is injected from the bottom (or water is injected from the top), the gas (water) is a segmented flow to form a series of bubbles (droplets). When the LCN is small, the gas (water) separates a series of small bubbles (droplets) and then flows out of the vug after sequentially entering the vug, and the displacement efficiency is as small as 10% or less. When the LCN is larger, a number of large bubbles (droplets) enter the vug, causing the top oil to fluctuate, and the oil flows out of the vug with the gas (water), so that displacement efficiency is increased.

Effect of gravity factor. For the horizontal model setup, the results of water flooding and gas injection are similar without considering gravity. However, for the vertical model setup, gravity acts significantly on the results of water flooding and gas injection. Because the oil-gas density difference is much larger than the oil-water density difference, gas is more susceptible to gravity. The remaining oil is mainly distributed above the horizontal midline (water injection) or above the horizontal midline (gas injection). Then, gravity exerts a great influence on the morphology of bubbles. The bubble flows like a class of flat parabolic motion in the vug, and the diameter of the bubble is related to the width of the fracture and the injection velocity, irrespective of the shape of the vug. Overall, the larger is the fracture width and the higher is the gas injection velocity, the larger is the bubble size. In the case of water being injected, when the LCN is small, the water is separated into droplets after entering the vug. As the velocity increases, the water flows continuously.

Effect of outlet position. Through an analysis of the results, in the case of water being injected, when the outlet position is in the middle of the vug, the recovery factor is approximately 50%; when the outlet position is at the top of the vug, the recovery factor is close to 100%; and when the outlet position is at the bottom of the vug, the recovery rate is close to zero. Similarly, in the case of gas injection, when the outlet position is in the middle of the vug, the recovery factor is approximately 50%; when the outlet position is at the top of the vug, the recovery factor is close to zero; and when the outlet position is at the bottom of the vug, the recovery rate is close to 100%. The outlet position determines the displacement efficiency. We could predict that when water is flooding, the height of the outlet position is positively correlated with the recovery factor. Overall, the higher is the outlet position, the higher is the recovery rate. However, when gas is injected, the height of the outlet position is inversely related to the recovery factor. In general, the lower is the outlet position, the higher is the recovery rate. In practice, water is preferably injected from the bottom, while gas is preferably injected from the top. If water is injected from the top or gas is injected from the bottom, it is necessary to increase the water or gas injection velocity in order to increase oil recovery.

Effect of shape factor. For the horizontal model setup, the remaining oil of the square model is primarily distributed at four corners, and the remaining oil of the spherical model is mainly away from the horizontal midline. After water or gas is continuously injected, the oil phase velocity field of the remaining oil region cannot fluctuate. For the vertical model setup, when water is injected from the bottom or gas is injected from the top, the outlet of the spherical model is convergent, while the outlet of the square model is suddenly smaller, resulting in slightly higher recovery efficiency in

the spherical model than in the square model. In contrast, when water is injected from the top or gas is injected from the bottom, the square model is superior to the spherical model. This is because the top of the square model (bottom) has a "block" at the top of the contour to increase displacement efficiency, while the top (bottom) of the spherical model assumes a "converged" shape, thus causing water or gas to flow out easily.

4. Conclusions

In this work, based on 3D printing technology, we designed and constructed a set of visualization multiphase flow experiment systems for multiphase flow in fracture-vug medium. By combining BVM and PIV methods, we conducted multiphase flow experimental tests. Based on the experimental results, the influence of crucial parameters on multiphase flow in fracture-vug medium is analyzed. The main findings are as follows:

1. For a horizontal model setup, the smaller is the LCN, the more gas or water could displace the oil away from the horizontal midline region, resulting in greater sweep efficiency. For a vertical model setup, as fracture dip angle $\omega \approx 0$, within a certain range of LCN, the displacement efficiency does not change substantially in the case of gas injection. However, in the case of water injection, when the LCN is small, water could drive some oil near the horizontal midline. In addition, when the LCN is larger, the water phase velocity field shrinks toward the horizontal midline, which leads to a decrease in displacement efficiency. As fracture dip angle $\omega \approx \pi/2$, if gas is injected from the top (or water is injected from the bottom), the gas (water) appears as a piston flow; and the larger is the LCN, the smaller is the Se. If gas is injected from the bottom (or water is injected from the top), gas (water) is a segmented flow to form a series of bubbles (droplets); and the larger is the LCN, the larger is the Se.
2. Gravity has a great influence on the morphology of bubbles in the case of gas injection. The diameter of the bubble is related to the width of the fracture and the injection velocity, irrespective of the shape of the vug. However, in the case of water injection, when the LCN is small, the water is separated into droplets after entering the vug. As the velocity increases, the water flows continuously.
3. The outlet position determines the displacement efficiency. In the case of water flooding, the height at the outlet position is positively correlated with the recovery factor. However, in the gas injection, the height at the outlet position is inversely related to the recovery factor. In practice, water is preferably injected from the bottom, while gas is preferably injected from the top.
4. The shape of the vug has an effect on the distribution of the remaining oil and oil recovery. For a horizontal model setup, the remaining oil of the square model is mainly distributed at four corners, and the remaining oil of the spherical model is mainly away from the horizontal midline. For a vertical model setup, when water is injected from the bottom or gas is injected from the top, there is a slightly higher recovery efficiency in the spherical model than in the square model. In contrast, when water is injected from the top or gas is injected from the bottom, the square model is superior to the spherical model.

This study also provides a set of experimental results that may be useful for theoretical study and numerical simulation of multiphase flow in fractured-vuggy medium. However, certain issues should be addressed in future studies. For instance, the surface of the 3D printing model is easy to adsorb fluorescent particles. The accuracy of PIV experiments would then be reduced if the 3D printing physical model is used many times. In addition, the fracture-vug structure is relatively simple in this work. Multi-phase fluid flow in complex fracture-vug combinations and fracture-vug filled models constitutes an interesting and challenging topic, and corresponding work is ongoing.

Acknowledgement

This work is supported by the National Science and Technology Major Project (Grant No. 2016ZX05014-004-006).

Nomenclature

u = fluid velocity, $m \cdot s^{-1}$
ρ = fluid density, $Kg \cdot m^{-3}$
μ = fluid viscosity, $mPa \cdot s$
L = characteristic length of the reservoir's thickness, m
χ = the ratio of pressure to gravity
g = gravity, $m \cdot s^{-2}$
Δp = pressure difference, Pa
e = the parameters in the physical model
D_v = the diameter of vug, m
W_f = the opening of fracture, m
v = the flow rate, m/s
Q = the injection speed, m^3/d
n_f = the fracture density, m^{-1}
ξ = the coordination number
η = the filling degree, %
V_{vug} = the volume of vug, m^3
kx_f = the conductivity of fracture, m^3
r_w = the wellbore radius, m
u_p = particle velocity, $m \cdot s^{-1}$
ρ_p = particle density, $Kg \cdot m^{-3}$
d_p = the diameter of particle, m
t = the time, s
T = the delay time, s
k = the reciprocal of T, $1/s$
ω = fracture dip angle
Se = sweep efficiency
PV = pore volume
LCN = a logarithm of the capillary number
σ = interfacial tension, $N \cdot m^{-1}$

References

Ahmadi, M.A., Shadizadeh, S.R., 2013. Implementation of a high-performance surfactant for enhanced oil recovery from carbonate reservoirs. Journal of Petroleum Science and Engineering 110, 66-73. https://doi.org/10.1016/j.petrol.2013.07.007.

Arbogast, T., Brunson, D.S., 2007. A computational method for approximating a Darcy–Stokes system governing a vuggy porous medium. Computational Geosciences 11, 207-218. DOI:10.1007/s10596-007-9043-0.

Arbogast, T., Lehr, H.L., 2006. Homogenization of a Darcy–Stokes system modeling vuggy porous media. Computational Geosciences 10, 291-302. DOI 10.1007/s10596-006-9024-8.

Basset, A., 1961. A Treatise on Hydrodynamics, vol. 2. Deighton, Bell and Company. reprinted by Dover.

Camacho Velazquez, R., Vasquez-Cruz, M.A., Castrejon-Aivar, R., Arana-Ortiz, V., 2002. Pressure transient and decline curve behaviors in naturally fractured vuggy carbonate reservoirs. SPE Annual Technical Conference and Exhibition. https://doi.org/10.2118/77689-MS.

Chang, L.-C., Tsai, J.-P., Shan, H.-Y., Chen, H.-H., 2009. Experimental study on imbibition displacement mechanisms of two-phase fluid using micro model. Environmental Earth Sciences 59, 901. DOI:10.1007/s12665-009-0085-6.

Chen, C., Mehl, B.T., Munshi, A.S., Townsend, A.D., Spence, D.M., Martin, R.S., 2016. 3D-printed microfluidic devices: fabrication, advantages and limitations—a mini review. Analytical Methods 8, 6005-6012. DOI:10.1039/C6AY01671E.

Cheng, J.T., Pyrak- Nolte, L.J., Nolte, D.D., Giordano, N.J., 2004. Linking pressure and saturation through interfacial areas in porous media. Geophysical Research Letters 31. https://doi.org/10.1029/2003GL019282.

Cottin, C., Bodiguel, H., Colin, A., 2010. Drainage in two-dimensional porous media: From capillary fingering to viscous flow. Physical Review E 82, 046315. https://doi.org/10.1103/PhysRevE.82.046315.

Cruz-Hernandez, J., Islas-Juarez, R., Perez-Rosales, C., Rivas-Gomez, S., Pineda-Munoz, A., Gonzalez-Guevara, J., 2001. Oil displacement by water in vuggy fractured porous media, SPE Latin American and Caribbean Petroleum Engineering Conference. Society of Petroleum Engineers. https://doi.org/10.2118/69637-MS.

Dabbouk, C., Liaqat, A., Williams, G., Beattie, G., 2002. Waterflood in vuggy layer of a middle east reservoir-displacement physics understood, Abu Dhabi International Petroleum Exhibition and Conference. Society of Petroleum Engineers. https://doi.org/10.2118/78530-MS.

Dong, Z., Aifen, L., Jun, Y., Zhanguo, L., Yanqing, F., Qiang, S., 2011. A single-phase fluid flow pattern in a kind of fractured-vuggy media. Petroleum Science and Technology 29, 1030-1040. https://doi.org/10.1080/10916466.2011.553657.

Ferer, M., Ji, C., Bromhal, G.S., Cook, J., Ahmadi, G., Smith, D.H., 2004. Crossover from capillary fingering to viscous fingering for immiscible unstable flow: Experiment and modeling. Physical Review E 70, 016303. https://doi.org/10.1103/PhysRevE.70.016303.

He, J., Tang, H., Wang, C., 2017. Characteristics of water flooding for fractured-cavity carbonate reservoirs with CFD method. Electronic Journal of Geotechnical Engineering 22, 1823-1834.

Hou, J., LI, H., Jiang, Y., Luo, M., Zheng, Z., Zhang, L., Yuan, D., 2014. Macroscopic three-dimensional physical simulation of water flooding in multi-well fracture-cavity unit. Petroleum Exploration & Development 41, 784-789. DOI: 10.11698/PED.2014.06.10.

Hui, J., Liu, X., Wang, Y., 2015. Mechanism and practice of nitrogen injection for EOR in fractured-vuggy carbonate reservoir in Tahe Oilfield, Tarim Basin. Xinjiang Petroleum Geology 36, 75-77. DOI：10.7657/XJPG20150114.

Ishutov, S., Hasiuk, F.J., Harding, C., Gray, J.N., 2015. 3D printing sandstone porosity models. Interpretation 3, SX49-SX61. https://doi.org/10.1190/INT-2014-0266.1.

Ju, Y., Xie, H., Zheng, Z., Lu, J., Mao, L., Gao, F., Peng, R., 2014. Visualization of the complex structure and stress field inside rock by means of 3D printing technology. Chinese Science Bulletin 59, 5354-5365. DOI:10.1007/s11434-014-0579-9.

Karimaie, H., Darvish, G.R., Lindeberg, E., Torsæter, O., 2008. Secondary and tertiary gas injection in fractured carbonate rock: Experimental study. Journal of Petroleum Science and Engineering 62, 45-51. https://doi.org/10.1016/j.petrol.2008.07.007.

Lenormand, R., Touboul, E., Zarcone, C., 1988. Numerical models and experiments on immiscible displacements in porous media. Journal of Fluid Mechanics 189, 165-187. https://doi.org/10.1017/S0022112088000953.

Lifton, V.A., 2016. Microfluidics: an enabling screening technology for enhanced oil recovery (EOR). Lab on a Chip 16, 1777-1796. DOI:10.1039/C6LC00318D.

Lv, A., Yao, J., Wang, W., 2011. Characteristics of oil-water relative permeability and influence mechanism in fractured-vuggy medium. Procedia Engineering 18, 175-183. https://doi.org/10.1016/j.proeng.2011.11.028.

Lyu, X., Liu, Z., Hou, J., Lyu, T., 2017. Mechanism and influencing factors of EOR by N2 injection in fractured-vuggy carbonate reservoirs. Journal of Natural Gas Science and Engineering 40, 226-235. https://doi.org/10.1016/j.jngse.2017.02.022.

Mohsenzadeh, A., Escrochi, M., Afraz, M.V., Karimi, G., Al-Wahaibi, Y., Ayatollahi, S., 2016. Non-hydrocarbon gas injection followed by steam–gas co-injection for heavy oil recovery enhancement from fractured carbonate reservoirs. Journal of Petroleum Science and Engineering 144, 121-130. https://doi.org/10.1016/j.petrol.2016.03.003.

Peng, X., Du, Z., Liang, B., Qi, Z., 2009. Darcy-stokes streamline simulation for the tahe-fractured reservoir with cavities. SPE Journal 14, 543-552. https://doi.org/10.2118/107314-PA.

Rezaei, N., Mohammadzadeh, O., James, L.A., Chatzis, I., 2013. Experimental investigation of the VAPEX process in vuggy porous media. SPE Journal 19, 101-108. https://doi.org/10.2118/163106-PA.

Willingham, T.W., Werth, C.J., Valocchi, A.J., 2008. Evaluation of the effects of porous media structure on mixing-controlled reactions using pore-scale modeling and micromodel experiments. Environmental Science & Technology 42, 3185-3193. https://doi.org/10.1021/es7022835.

Wu, M., Xiao, F., Johnson-Paben, R.M., Retterer, S.T., Yin, X., Neeves, K.B., 2012. Single-and two-phase flow in microfluidic porous media analogs based on Voronoi tessellation. Lab on a Chip 12, 253-261. DOI:10.1039/C1LC20838A.

Wu, Y.-S., Di, Y., Kang, Z., Fakcharoenphol, P., 2011. A multiple-continuum model for simulating single-phase and multiphase flow in naturally fractured vuggy reservoirs. Journal of Petroleum Science and Engineering 78, 13-22. https://doi.org/10.1016/j.petrol.2011.05.004.

Xie, H., Li, A., Huang, Z., Gao, B., Peng, R., 2017. Coupling of two-phase flow in fractured-vuggy reservoir with filling medium. Open Physics 15, 12-17. https://doi.org/10.1515/phys-2017-0002.

Yang, L., 2012. Ordovician carbonate fracture-cavity reservoirs identification and quantitative characterization in Tahe Oilfield [J]. Journal of China University of Petroleum (Edition of Natural Science) 1. DOI:10.3969/j.issn.1673-5005.2012.01.001.

Yao, J., Huang, Z.-Q., 2017. Fractured Vuggy Carbonate Reservoir Simulation. Springer.

Zhang, C., Dehoff, K., Hess, N., Oostrom, M., Wietsma, T.W., Valocchi, A.J., Fouke, B.W., Werth, C.J., 2010. Pore-scale study of transverse mixing induced CaCO3 precipitation and permeability reduction in a model subsurface sedimentary system. Environmental Science & Technology 44, 7833-7838. https://doi.org/10.1021/es1019788.

Zhang, C., Oostrom, M., Wietsma, T.W., Grate, J.W., Warner, M.G., 2011. Influence of viscous and capillary forces on immiscible fluid displacement: Pore-scale experimental study in a water-wet micromodel demonstrating viscous and capillary fingering. Energy & Fuels 25, 3493-3505. https://doi.org/10.1021/ef101732k.

Figure Captions

Fig. 1. Different study views of spherical and square models. The first two columns are the case in which the fracture dip angle is approximately 0 in the horizontal and vertical section of the model, respectively; the third column is the case in which the fracture dip angle is approximately $\pi/2$ in the vertical section of the model.

Fig. 2. Schematic diagrams of the fracture-vug model: (a) spherical model; (b) square model. The black dotted line is the horizontal midline, and the yellow dotted line is the vertical midline. The gray area is the entirety of fracture-vug medium of the field of view (FOV); the green area is the inlet of the FOV; and the red area is the outlet of the FOV.

Fig. 3. Physical fracture-vug model by 3D printing. (a) Spherical model; (b) square model.

Fig. 4. (a) The Stratasys Objet350 Connex3 3D printer (limit resolution: 16 μm/30 μm; maximum size: 340×340×200 mm^3); (b) schematic diagram of 3D printing-PolyJet.

Fig. 5. Wettability of the physical model, in which gray is the water phase, transparent is the oil phase, and the circle is the gas phase. (a) The contact angle of the oil-gas-water uncoated model; (b) the contact angle of the oil-gas-water coated model.

Fig. 6. Streamline diagram of the fracture-vug system multiphase flow visualization platform.

Fig. 7. Multiphase flow visualization platform for the fracture-vug system: (a) injection system and control system; (b) control and data acquisition system; (c) optical platform system.

Fig. 8. Procedure of the experiment.

Fig. 9. The process of LED BVM for multiphase flow: (a) calibration; (b) water injection; (c) gas injection.

Fig. 10. The process of the PIV method for multiphase flow: (a) oil and water after adding the fluorescent particles; (b) after laser excitation of the fluorescent particles; (c) optical micrograph of the fluorescent particles (X1000); (d) the optical platform system.

Fig. 11. Results of horizontal gas-oil experiments at different gas injection velocities in the spherical model or the square model, where red is oil and green is gas. a_i-d_i (A_i-D_i) (i=1-3) represent the oil-gas saturation distribution in the spherical (square) model when gas is injected at 0.1, 0.3, 0.5, and 1 PV, respectively. The lower indices 1, 2, and 3 indicate that the gas injection velocity LCN is -6, -5, and -4, respectively.

Fig. 12. Displacement efficiency statistics of horizontal gas-oil experiments with different gas injection velocities at different gas injection pore volumes in the spherical model or in the square model.

Fig. 13. Results of vertical gas-oil experiments at different gas injection velocities in the spherical model or the square model, where red is oil and green is gas. a_i-e_i (A_i-E_i) (i=1-3) represent the oil-gas saturation distribution in the spherical (square) model when gas is injected at 0.05, 0.15, 0.3, 0.45, and 0.8 PV, respectively. The lower indices 1, 2, and 3 indicate that the gas injection velocity LCN is -6, -5, and -4, respectively.

Fig. 14. Displacement efficiency statistics of vertical gas-oil experiments with different gas injection velocities at different gas injection pore volumes in the spherical model or the square model.

Fig. 15. Results of vertical water-oil experiments at different water injection velocities in the spherical model or the square model, where red is oil and blue is water. A_i-E_i (a_i-e_i) (i=0-2) represent the oil-water saturation distribution in the square (spherical) model when water is injected at 0.08, 0.26, 0.42, 0.52, and 0.8 PV, respectively. The lower indices 0, 1, and 2 indicate that the water injection velocity LCN is -4.3, -3.3, and -2.3, respectively.

Fig. 16. Displacement efficiency statistics of vertical water-oil experiments with different water injection velocities at different water injection pore volumes in the spherical model and in the square model.

Fig. 17. Results of vertical gas-oil experiments at different gas injection velocities in which the gas is injected from the top, where red is oil and green is gas. A_1-E_1(a_1-e_1) represent the oil-gas saturation distribution in the square (spherical) model when gas is injected at 0.05, 0.3, 0.45, 0.75, and 1.05 PV, respectively. A_2-E_2(a_2-e_2) represent the oil-gas saturation distribution in the square (spherical) model when gas is injected at 0.1, 0.4, 0.6, 0.9, and 1.1 PV, respectively. The lower indices 1 and 2 indicate that the gas injection velocity LCN is -5 and -3.48, respectively.

Fig. 18. Displacement efficiency statistics of vertical gas-oil experiments for different models with gas being injected from the top: (a)

LCN= -5, gas injected from the top; (b) LCN= -3.48, gas injected from the top.

Fig. 19. Results of vertical gas-oil experiments at different gas injection velocities in which the gas is injected from the bottom, where red is oil and green is gas. A_1-E_1 (a_1-e_1) represent the oil-gas saturation distribution in the square (spherical) model when gas is injected at 0.05, 0.3, 0.55, 0.8, and 1.05 PV, respectively. A_2-E_2 (a_2-e_2) represent the oil-gas saturation distribution in the square (spherical) model when gas is injected at 0.1, 0.6, 1.1, 1.6, and 2.1 PV, respectively. The lower indices 1 and 2 indicate that the gas injection velocity LCN is -5 and -3.48, respectively.

Fig. 20. Displacement efficiency statistics of vertical gas-oil experiments for different models with gas being injected from the bottom: (a) LCN= -5, gas injected from the bottom; (b) LCN= -3.48, gas injected from the bottom.

Fig. 21. Results of vertical water-oil experiments at different water injection directions in the square model and the spherical model with LCN=-3.3, where red is oil and blue is water. A_1-E_1 (a_1-e_1) represent the oil-water saturation distribution in the square (spherical) model when water is injected at 0.05, 0.3, 0.6, 0.85, and 1.1 PV, respectively. A_2-E_2 (a_2-e_2) represent the oil-water saturation distribution in the square (spherical) model when water is injected at 0.1, 0.3, 0.6, 0.85, and 1.1 PV, respectively. The lower indices 1 and 2 indicate that water is injected from the bottom and top, respectively.

Fig. 22. Displacement efficiency statistics of vertical water-oil experiments at different water injection directions in the spherical model and in the square model: (a) LCN= -3.3, water injected from the bottom; (b) LCN= -3.3, water injected from the top.

Fig. 23. The oil phase velocity field in the spherical model at different oil injection velocities, where the flow direction is from left to right. a_i-d_i (i=1-3) represent the oil phase velocity field in the spherical model in which LCN is -6.38, -5.38, -4.38, and -3.48, respectively. The lower indices 1, 2, and 3 indicate that the FOV is the entire model, the inlet area, and the outlet area, respectively.

Fig. 24. The oil phase velocity field in the square model at different oil injection velocities, where the flow direction is from left to right. a_i-d_i (i=1-3) represent the oil phase velocity field in the square model in which LCN is -6.38, -5.38, -4.38, and -3.48, respectively. The lower indices 1, 2, and 3 indicate that the FOV is the entire model, the inlet area, and the outlet area, respectively.

Fig. 25. (a) is the magnification of Fig. 23(e_2); (b) is the magnification of Fig. 24(e_2).

Fig. 26. Horizontal flooding: oil-water velocity field when the LCN is -2.08 in different models, where the flow direction is from left to right and the red line is the oil-water interface. (a) In the spherical model; (b)-(c) In the square model ((b) is the oil-water velocity field during the water injection process, and (c) is the oil-water velocity field when the water is seen at the outlet).

Fig. 27. Vertical flooding: oil-water velocity field at different water injection velocities in the spherical model, where the flow direction is from left to right and the red line is the oil-water interface. (a)-(d): LCN is -3.68 ((a)-(d) are the oil-water velocity field at different water injection times: (a) is when the water just enters the vug; (b) is when the water reaches the bottom of the vug; (c) is when the water flows out of the vug; (d) is when the water is seen at the outlet); (e) LCN=-2.68; (f) LCN=-2.08. The green dotted region shows a reverse water velocity field in the lower horizontal line at the outlet end of the vug.

Fig. 28. Vertical flooding: oil-water velocity field at different water injection velocities in the square model, where the flow direction is from left to right and the red line is the oil-water interface. (a)-(c) LCN is -3.68 ((a)-(c) are the oil-water velocity field at different water injection times: (a) is when the water reaches the bottom of the vug; (b) is when the water is about to flow out of the vug; (c) is when the water is seen at the outlet).

Fig. 29. Horizontal flooding: oil-gas velocity field at different gas injection velocities in different models, where the flow direction is from left to right and the red line is the oil-gas interface. (a) The LCN is -4.38 in the spherical model; (b)-(d) the LCN is -5.38, -4.38, and -3.48 in the square model, respectively.

Fig. 30. Vertical flooding: oil-gas velocity field at different gas injection velocities in inlet FOV of the spherical model, where the flow direction is from left to right and the red line is the oil-gas interface. a_i-f_i are the oil-gas velocity field at different gas injection times, respectively. The lower indices 1, 2, and 3 indicate that the LCN is -5.38, -4.38, and -3.48, respectively.

List of Tables

Table 1 Similarity criteria in this study. Where ΔP is the pressure difference, Pa; ρ is the oil density, g/m^3; g is the gravity acceleration, m/s^2; L is the reservoirs thickness, m; μ is the oil viscosity, mPa·s; v is the flow rate, m/s; Q is the injection speed, m^3/d; n_f is the fracture density, m^{-1}; W_f is the opening degree of fracture, m; ξ is the coordination number; η is the filling degree, %; Vvug is the volume of vug, m^3; kx_f is the conductivity of fracture, m^3; r_w is the wellbore radius, m.

Type	No.	Similarity criteria	Remarks
Movement and dynamic similarities	1	$\Delta P / (\rho g L)$	Ratio of pressure to gravity
	2	$\mu / (\rho v L)$	Ratio of inertia resistance to viscous resistance (1/Re)
	3	$Q / (\rho v L^2)$	Ratio of injection to flow rate
	4	$(v\mu L) / (n_f W_f^3 \Delta P)$	Cubic law on multiple fractures
Geometric similarity	5	Ξ	Coordination number (the number of fractures connected by the reservoir (vug))
	6	η	Filling degree (the degree of filling in the vug)
	7	$V_{vug} / (kx_f)$	Ratio of vug volume to fracture conductivity
	8	r_w / L	Ratio of wellbore radius to reservoirs thickness (vug)

Table 2 Comparison of parameters in the reservoir model (Hou et al., 2014) and the physical model.

Parameters	Reservoir model	Physical model
Diameter of vug	1000-20000 mm	50 mm
Aperture of fracture	0.5-50 mm	0.5-2mm
Viscosity of crude oil	10-1000 mPa·s	20-500 mPa·s
Density of crude oil	0.92 g/cm^3	0.96 g/cm^3
Gravity	9.8 m/s^2	9.8 m/s^2
Difference of pressure	2-13 MPa	2.26-45.3 kPa
Velocity	30-150 m/d	0.002-1.67 m/s
Coordination number	1-5	2

Table 3 Properties of the experimental fluid (25℃, 1 atm).

Density (kg/m^3)	Water	1000
	Oil	960
	N_2	2
Viscosity (mPa·s)	Water	1
	Oil	20
	N_2	0.02
Interfacial tension (N/m)	N_2/water	0.072
	N_2/oil	0.02
	Oil/water	0.02

Table 4 Parameters of the fracture-vug model.

Facture-vug model	(a) Spherical model	(b) Square model
Size	*L*=100 mm, h=12 mm	*L*=100 mm, h=12 mm
D_v	50 mm	44.3 mm
W_f	0.5-2 mm	0.5-2 mm
H	2 mm	2 mm

Table 5 Change of Se with LCN under different conditions.

		Horizontal model	Vertical model	
			Oil-gas	Oil-water
Fracture dip angle ω≈0		The larger is the LCN, the smaller is the Se	Almost no effect of LCN on Se	The larger is the LCN, the smaller is the Se
Fracture dip angle $\omega\approx\pi/2$	Bottom	——	The larger is the LCN, the larger is the Se	The larger is the LCN, the smaller is the Se
	Top	——	Almost no effect of LCN on Se	The larger is the LCN, the larger is the Se

Figures

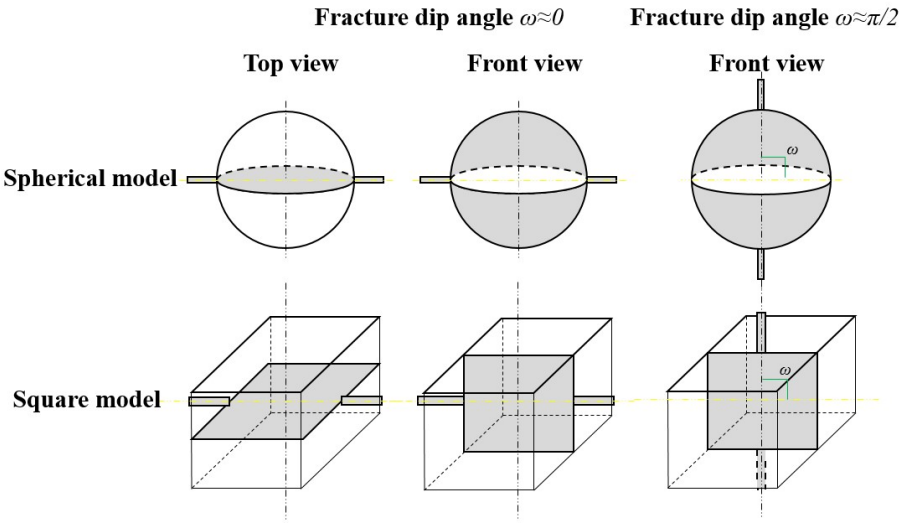

Fig. 1. Different study views of spherical and square models. The first two columns are the case in which the fracture dip angle is approximately 0 in the horizontal and vertical section of the model, respectively; the third column is the case in which the fracture dip angle is approximately π/2 in the vertical section of the model.

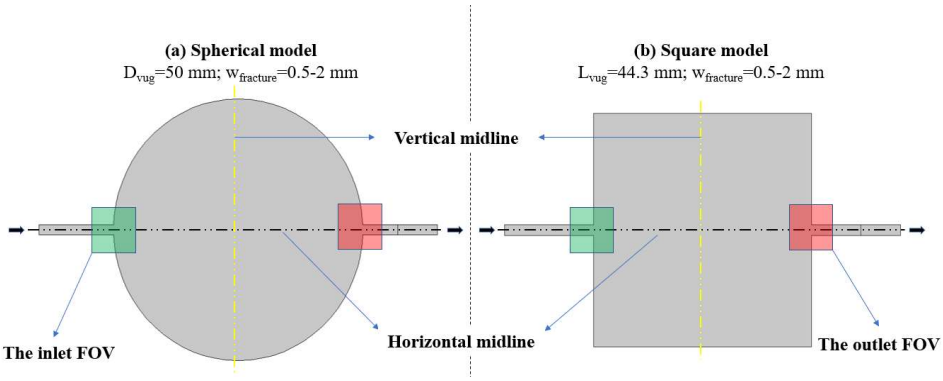

Fig. 2. Schematic diagrams of the fracture-vug model: (a) spherical model; (b) square model. The black dotted line is the horizontal midline, and the yellow dotted line is the vertical midline. The gray area is the entirety of fracture-vug medium of the field of view (FOV); the green area is the inlet of the FOV; and the red area is the outlet of the FOV.

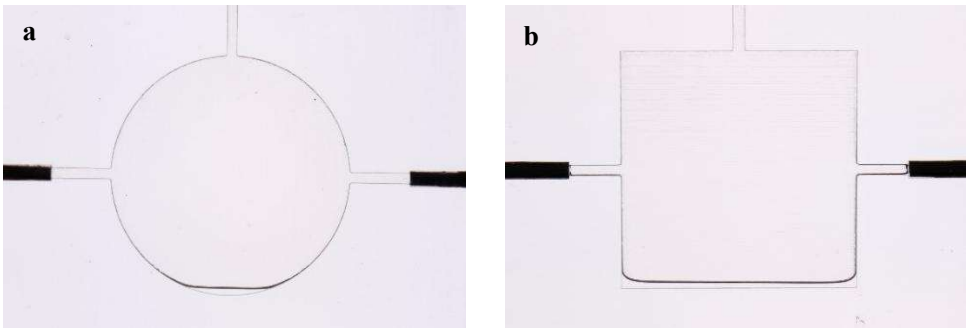

Fig. 3. Physical fracture-vug model by 3D printing. (a) Spherical model; (b) square model.

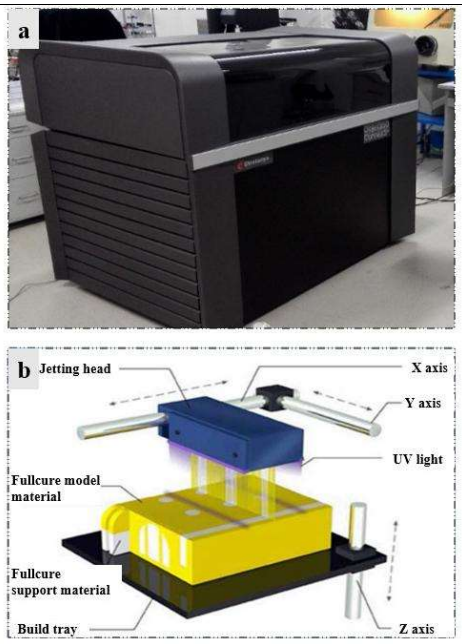

Fig. 4. (a) The Stratasys Objet350 Connex3 3D printer (limit resolution: 16 μm/30 μm; maximum size: 340×340×200 mm^3); (b) schematic diagram of 3D printing-PolyJet.

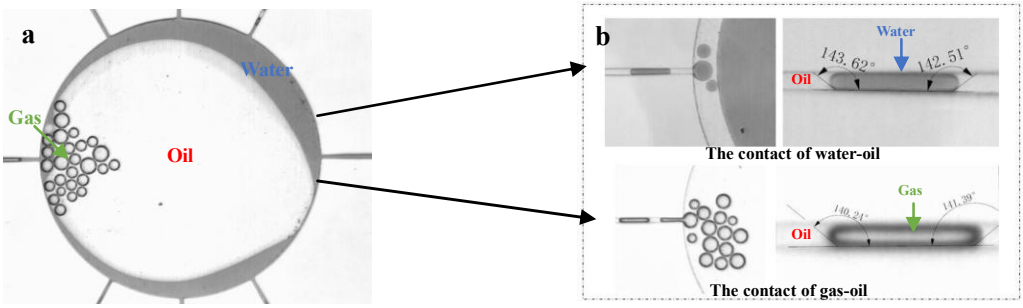

Fig. 5. Wettability of the physical model, in which gray is the water phase, transparent is the oil phase, and the circle is the gas phase. (a) The contact angle of the oil-gas-water uncoated model; (b) the contact angle of the oil-gas-water coated model.

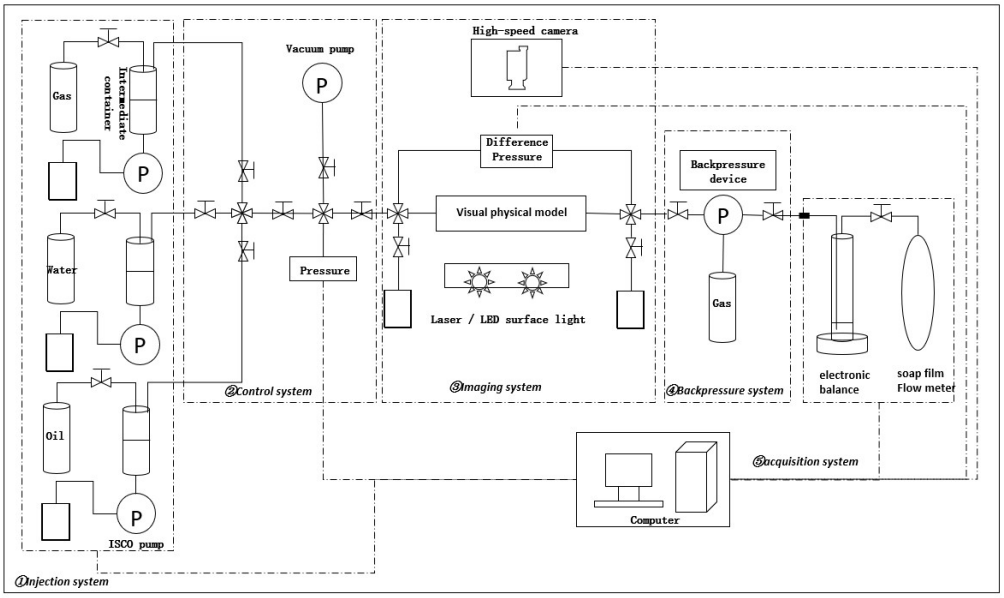

Fig. 6. Streamline diagram of the fracture-vug system multiphase flow visualization platform.

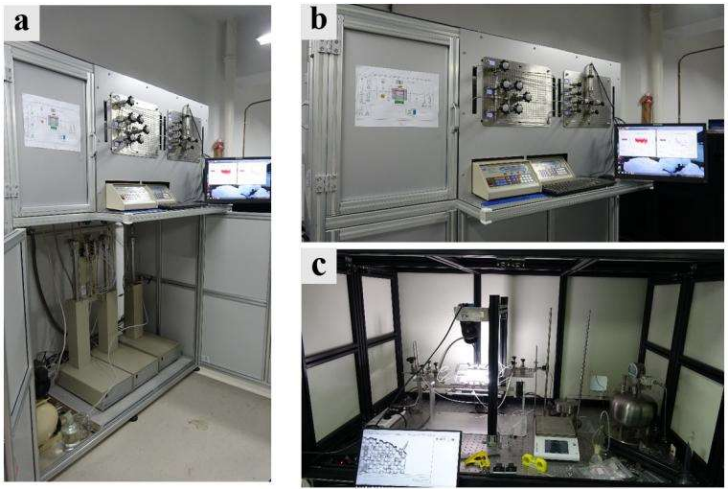

Fig. 7. Multiphase flow visualization platform for the fracture-vug system: (a) injection system and control system; (b) control and data acquisition system; (c) optical platform system.

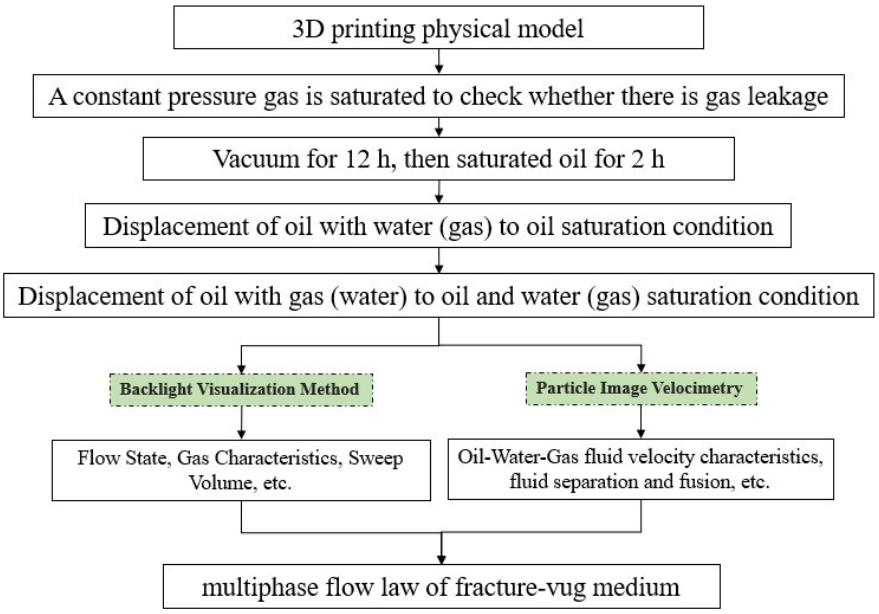

Fig. 8. Procedure of the experiment.

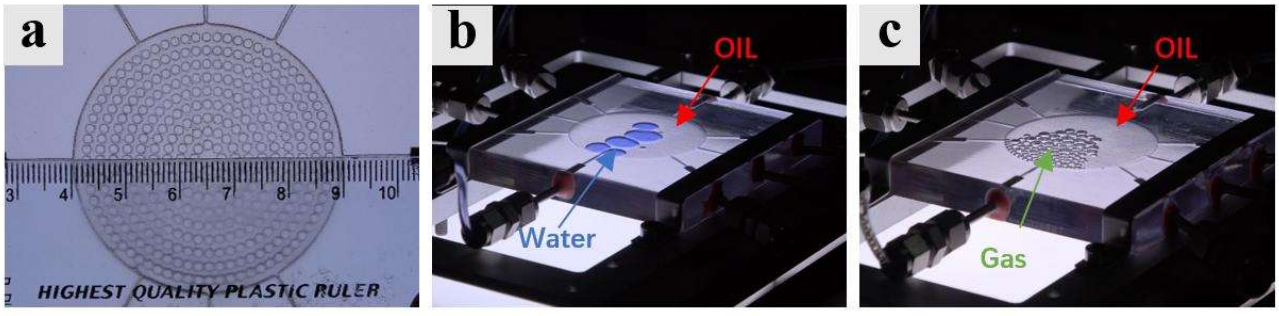

Fig. 9. The process of LED BVM for multiphase flow: (a) calibration; (b) water injection; (c) gas injection.

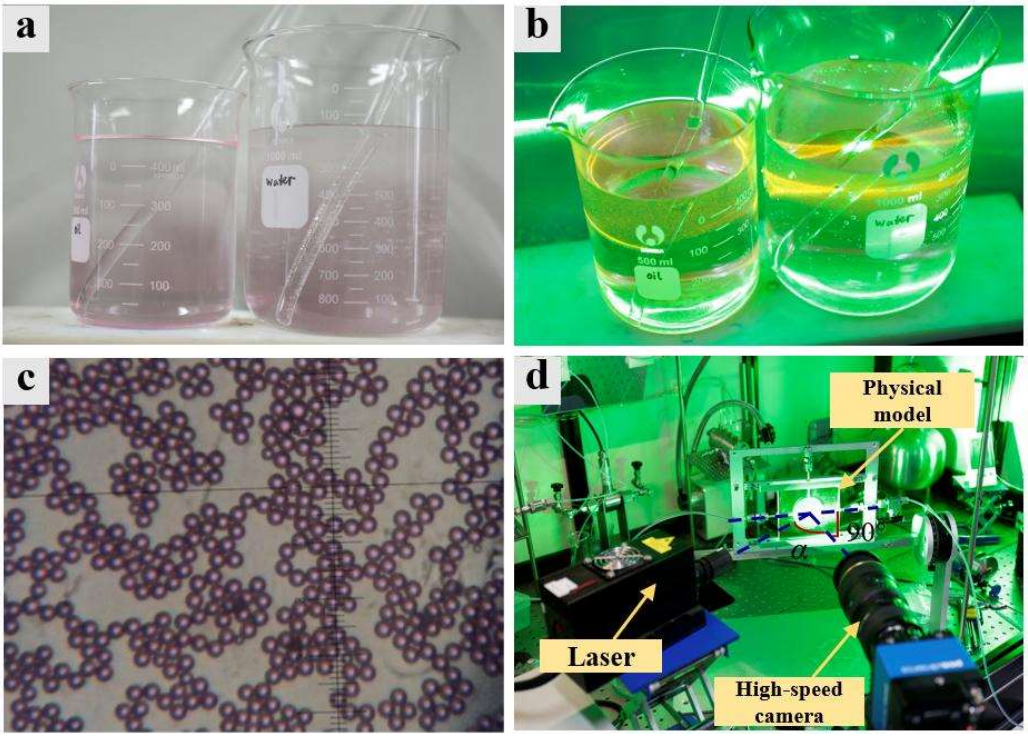

Fig. 10. The process of the PIV method for multiphase flow: (a) oil and water after adding the fluorescent particles; (b) after laser excitation of the fluorescent particles; (c) optical micrograph of the fluorescent particles (X1000); (d) the optical platform system.

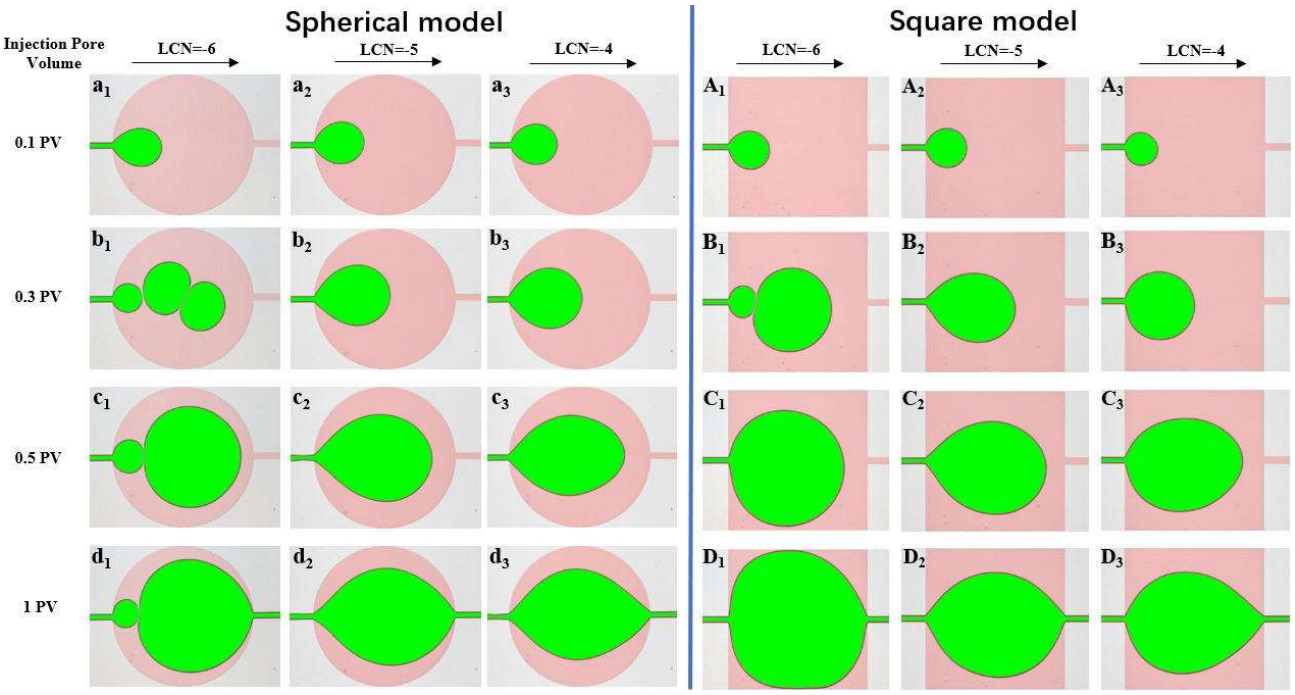

Fig. 11. Results of horizontal gas-oil experiments at different gas injection velocities in the spherical model or the square model, where red is oil and green is gas. a_i-d_i (A_i-D_i) (i=1-3) represent the oil-gas saturation distribution in the spherical (square) model when gas is injected at 0.1, 0.3, 0.5, and 1 PV, respectively. The lower indices 1, 2, and 3 indicate that the gas injection velocity LCN is -6, -5, and -4, respectively.

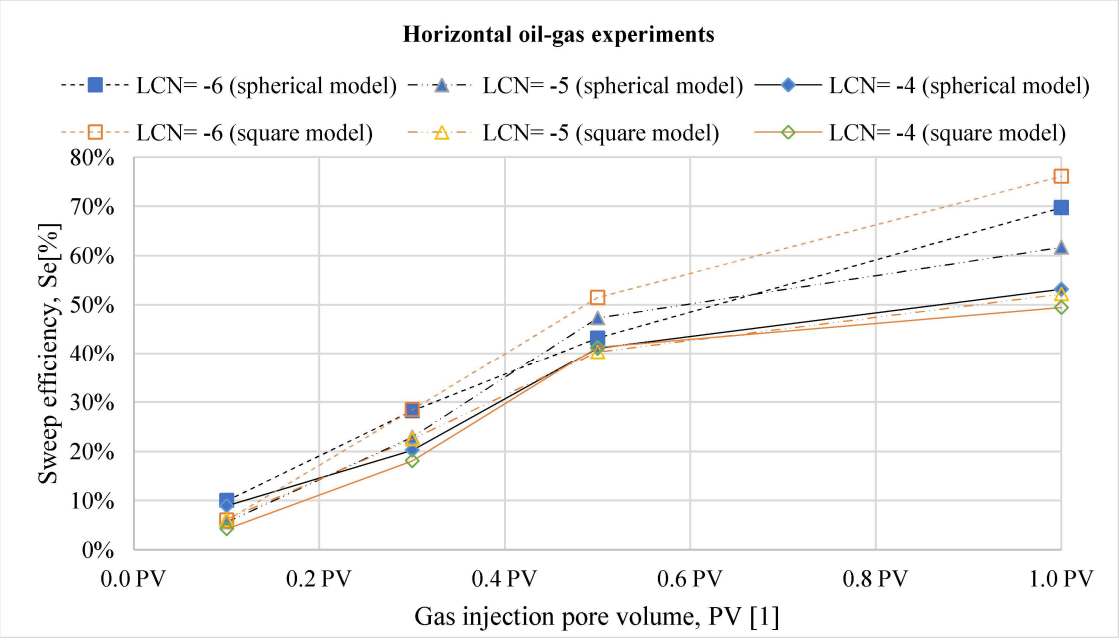

Fig. 12. Displacement efficiency statistics of horizontal gas-oil experiments with different gas injection velocities at different gas injection pore volumes in the spherical model or in the square model.

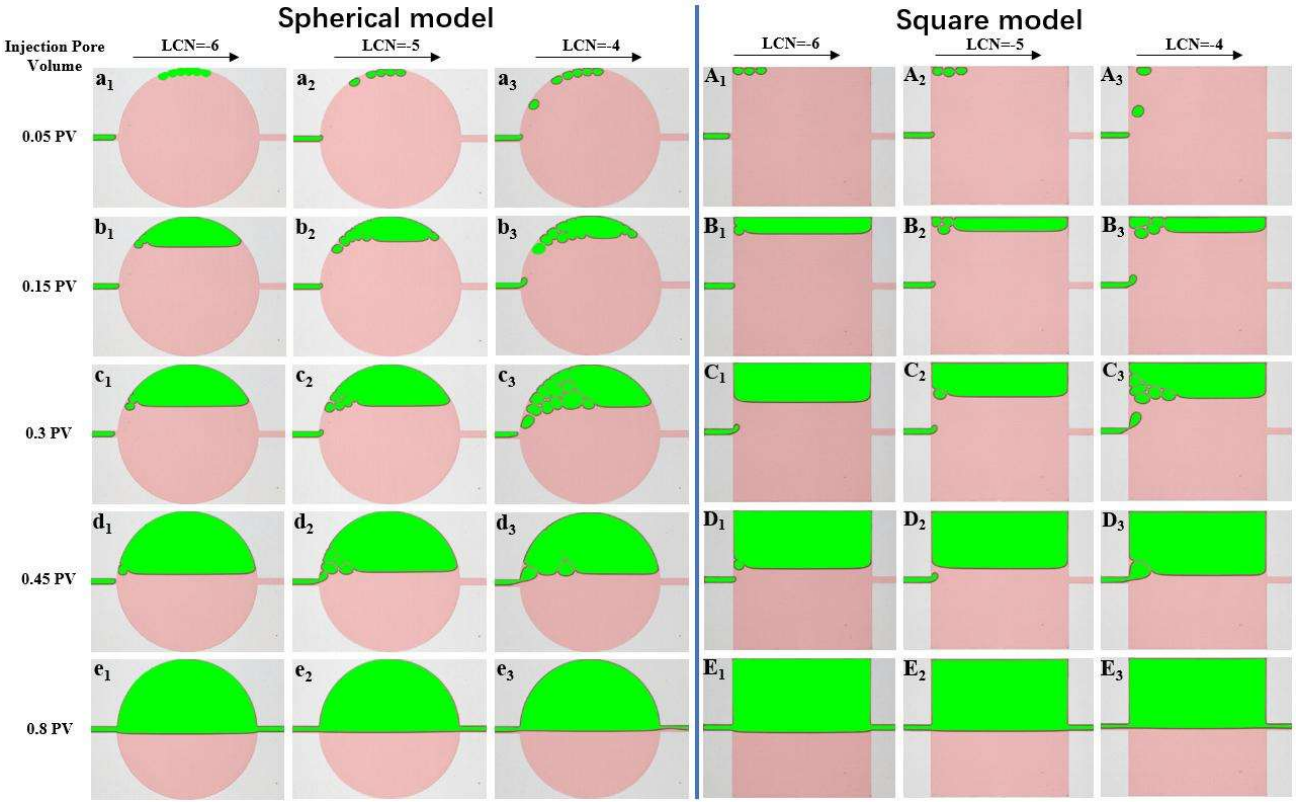

Fig. 13. Results of vertical gas-oil experiments at different gas injection velocities in the spherical model or the square model, where red is oil and green is gas. a_i-e_i (A_i-E_i) (i=1-3) represent the oil-gas saturation distribution in the spherical (square) model when gas is injected at 0.05, 0.15, 0.3, 0.45, and 0.8 PV, respectively. The lower indices 1, 2, and 3 indicate that the gas injection velocity LCN is -6, -5, and -4, respectively.

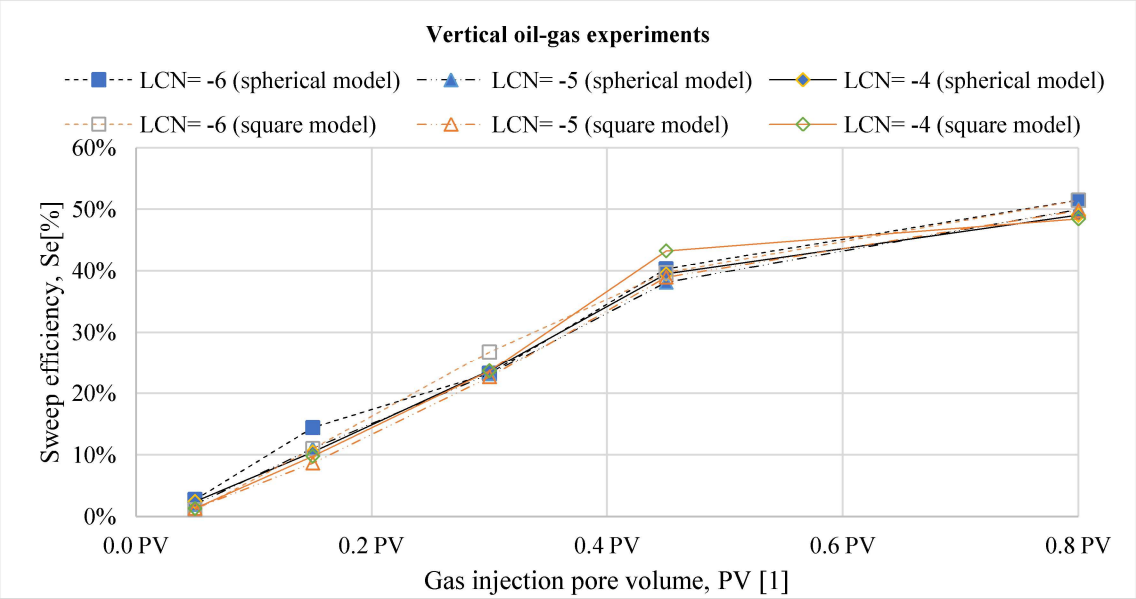

Fig. 14. Displacement efficiency statistics of vertical gas-oil experiments with different gas injection velocities at different gas injection pore volumes in the spherical model or the square model.

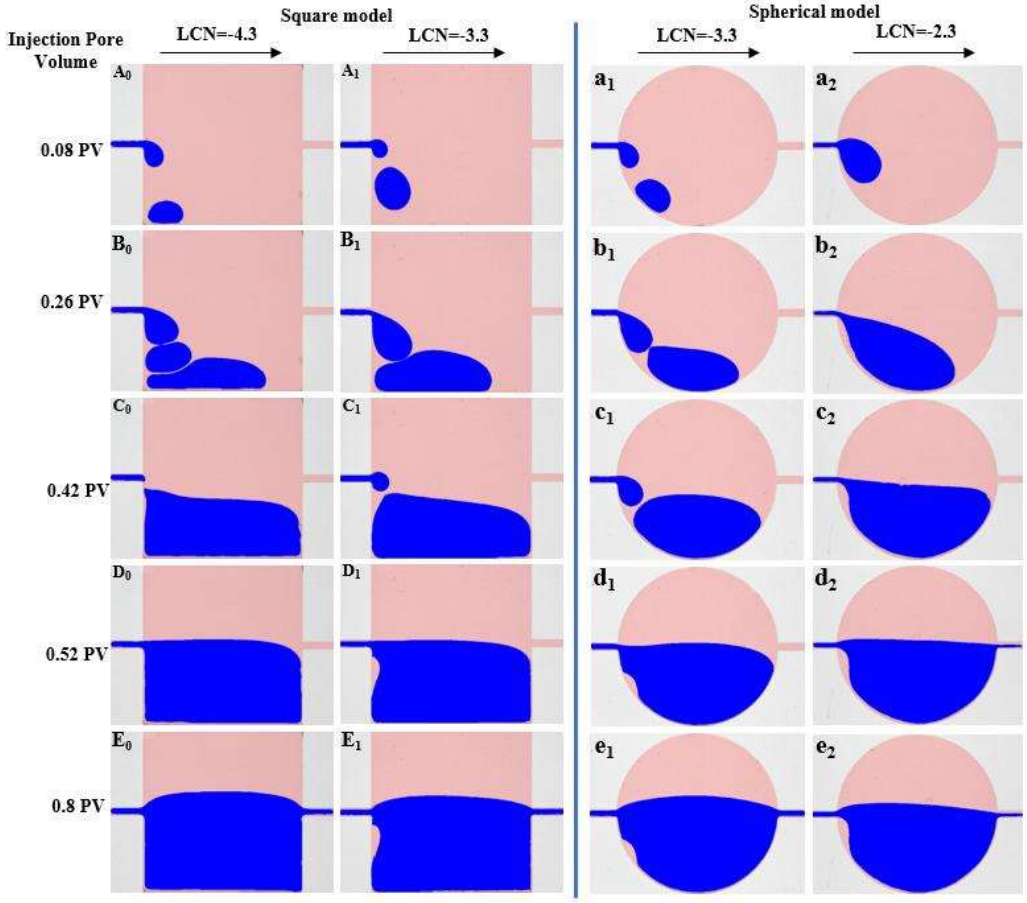

Fig. 15. Results of vertical water-oil experiments at different water injection velocities in the spherical model or the square model, where red is oil and blue is water. A_i-E_i (a_i-e_i) (i=0-2) represent the oil-water saturation distribution in the square (spherical) model when water is injected at 0.08, 0.26, 0.42, 0.52, and 0.8 PV, respectively. The lower indices 0, 1, and 2 indicate that the water injection velocity LCN is -4.3, -3.3, and -2.3, respectively.

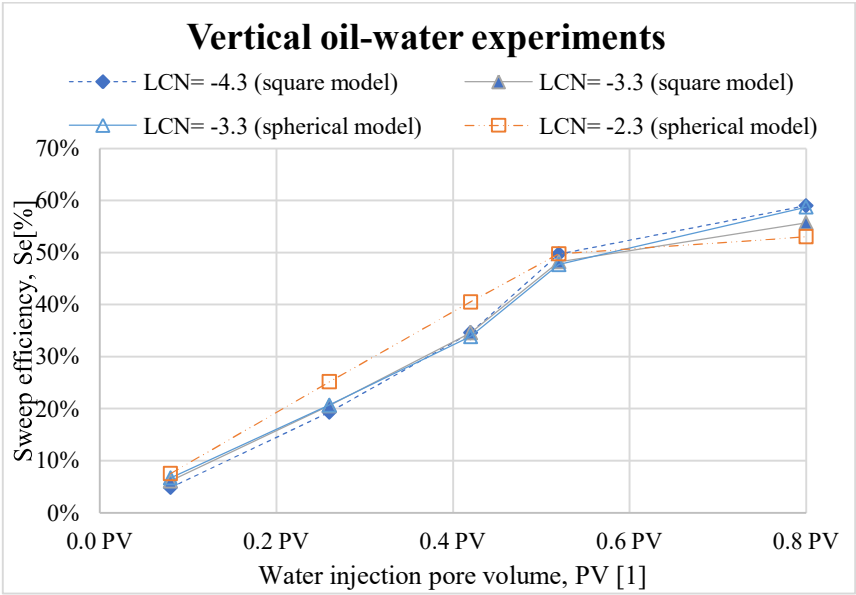

Fig. 16. Displacement efficiency statistics of vertical water-oil experiments with different water injection velocities at different water injection pore volumes in the spherical model and in the square model.

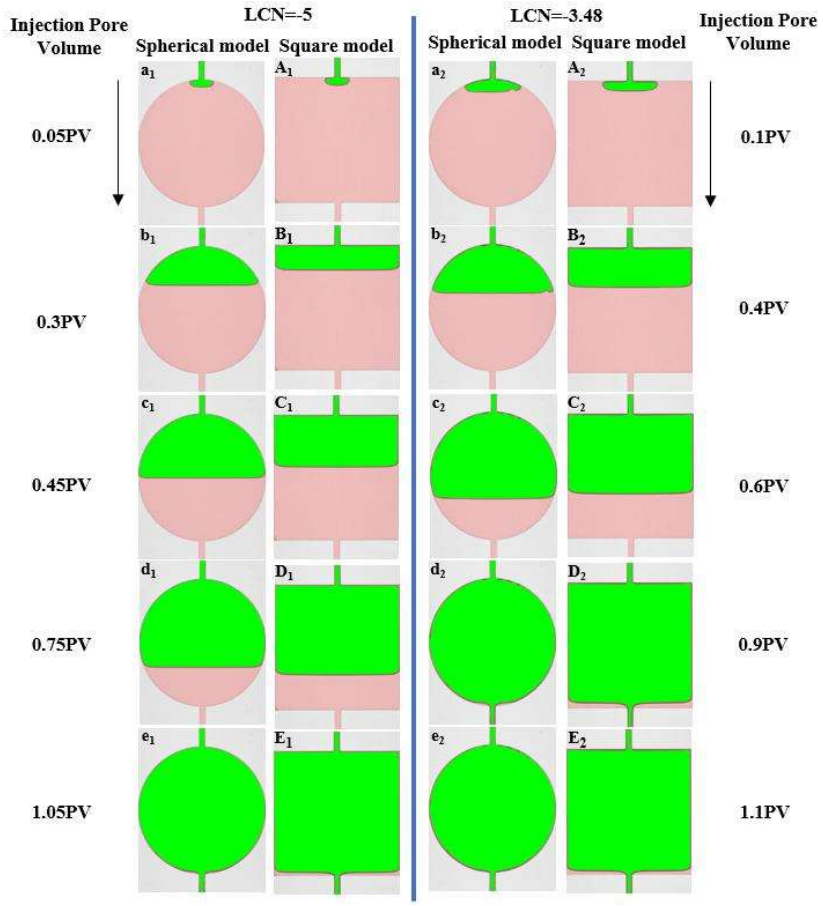

Fig. 17. Results of vertical gas-oil experiments at different gas injection velocities in which the gas is injected from the top, where red is oil and green is gas. A_1-E_1(a_1-e_1) represent the oil-gas saturation distribution in the square (spherical) model when gas is injected at 0.05, 0.3, 0.45, 0.75, and 1.05 PV, respectively. A_2-E_2(a_2-e_2) represent the oil-gas saturation distribution in the square (spherical) model when gas is injected at 0.1, 0.4, 0.6, 0.9, and 1.1 PV, respectively. The lower indices 1 and 2 indicate that the gas injection velocity LCN is -5 and -3.48, respectively.

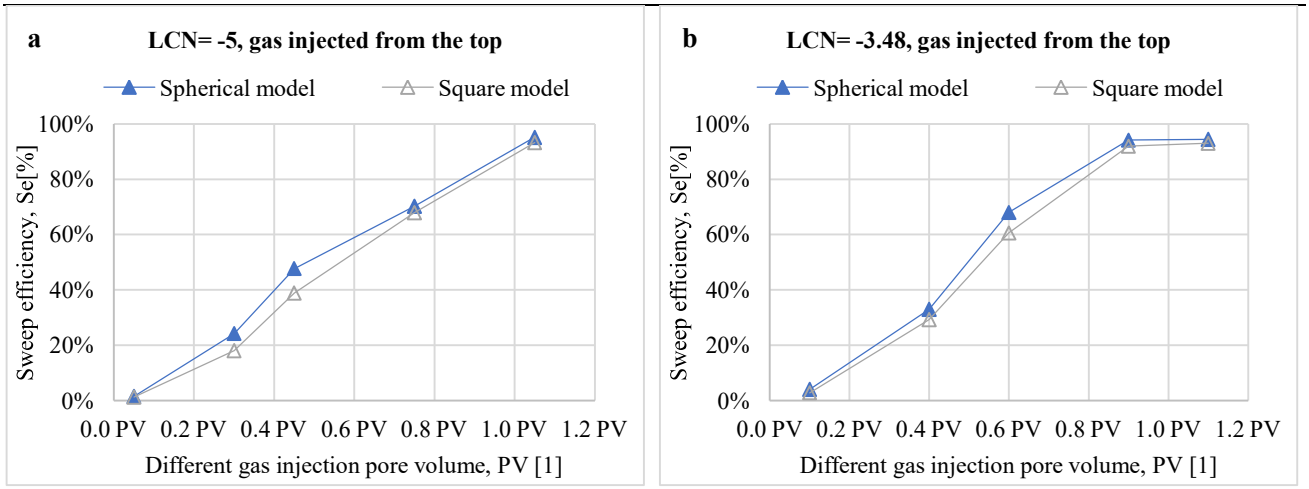

Fig. 18. Displacement efficiency statistics of vertical gas-oil experiments for different models with gas being injected from the top: (a) LCN= -5, gas injected from the top; (b) LCN= -3.48, gas injected from the top.

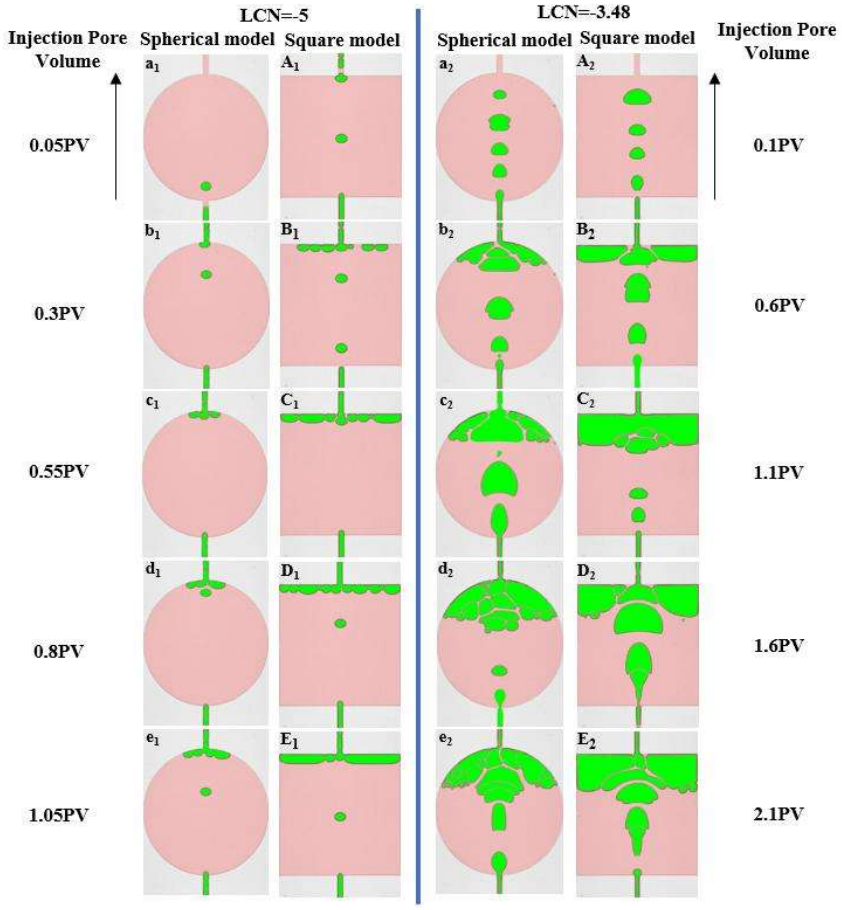

Fig. 19. Results of vertical gas-oil experiments at different gas injection velocities in which the gas is injected from the bottom, where red is oil and green is gas. A_1-E_1 (a_1-e_1) represent the oil-gas saturation distribution in the square (spherical) model when gas is injected at 0.05, 0.3, 0.55, 0.8, and 1.05 PV, respectively. A_2-E_2 (a_2-e_2) represent the oil-gas saturation distribution in the square (spherical) model when gas is injected at 0.1, 0.6, 1.1, 1.6, and 2.1 PV, respectively. The lower indices 1 and 2 indicate that the gas injection velocity LCN is -5 and -3.48, respectively.

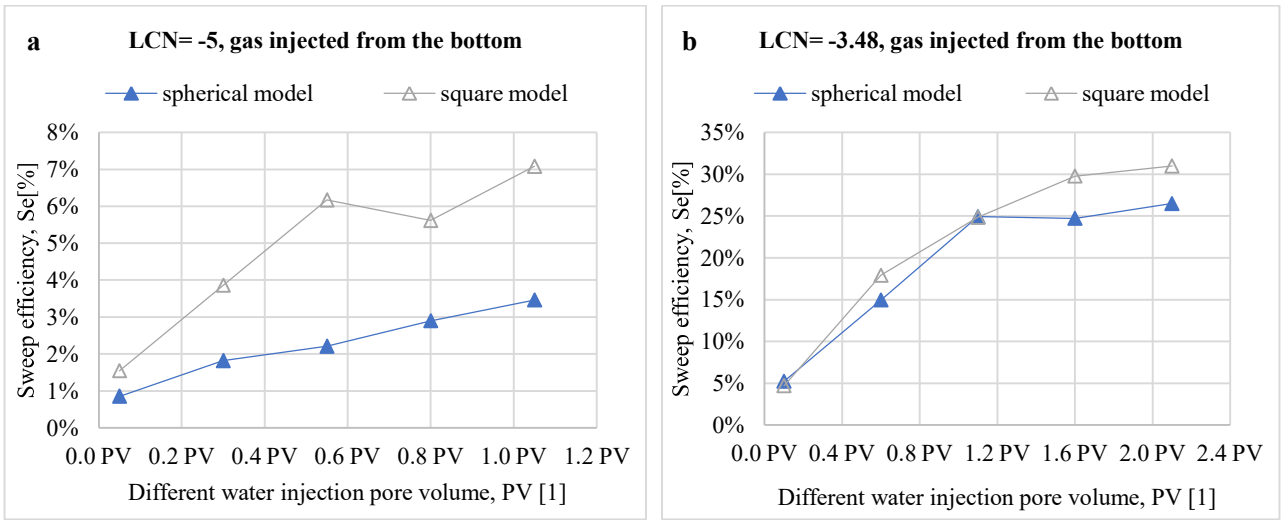

Fig. 20. Displacement efficiency statistics of vertical gas-oil experiments for different models with gas being injected from the bottom: (a) LCN= -5, gas injected from the bottom; (b) LCN= -3.48, gas injected from the bottom.

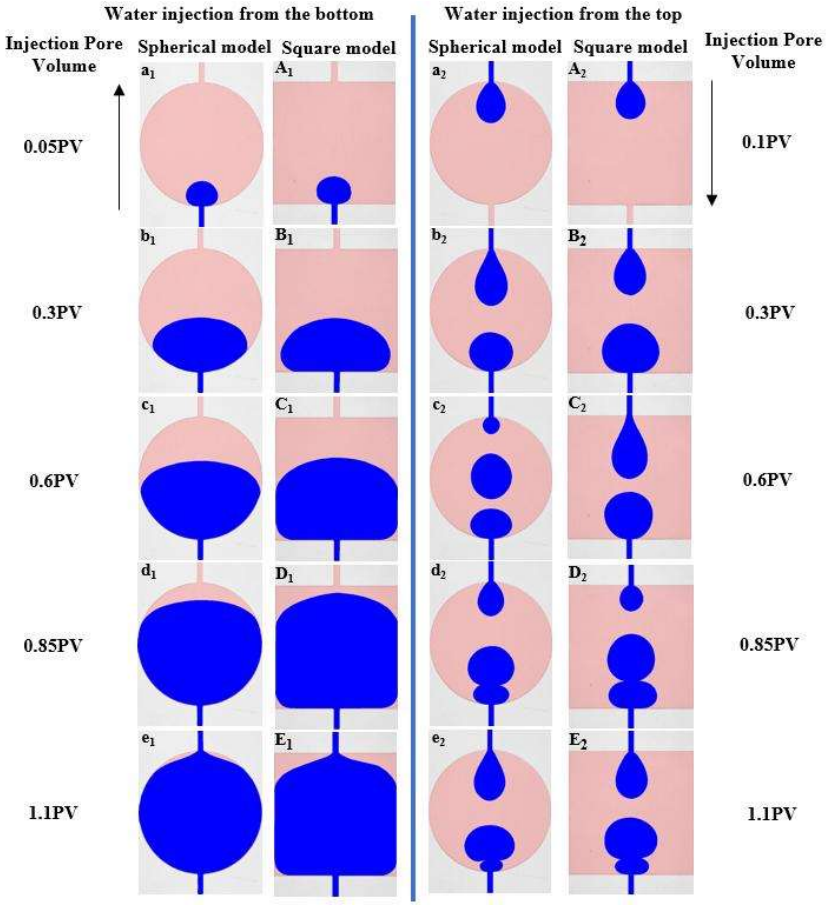

Fig. 21. Results of vertical water-oil experiments at different water injection directions in the square model and the spherical model with LCN=-3.3, where red is oil and blue is water. A_1-E_1 (a_1-e_1) represent the oil-water saturation distribution in the square (spherical) model when water is injected at 0.05, 0.3, 0.6, 0.85, and 1.1 PV, respectively. A_2-E_2 (a_2-e_2) represent the oil-water saturation distribution in the square (spherical) model when water is injected at 0.1, 0.3, 0.6, 0.85, and 1.1 PV, respectively. The lower indices 1 and 2 indicate that water is injected from the bottom and top, respectively.

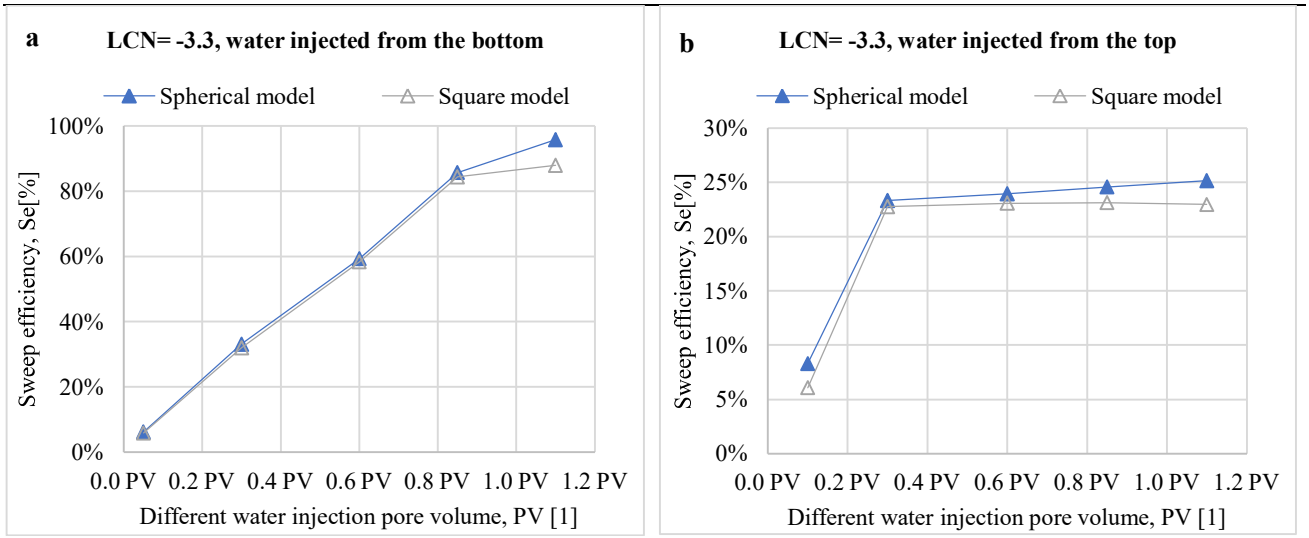

Fig. 22. Displacement efficiency statistics of vertical water-oil experiments at different water injection directions in the spherical model and in the square model: (a) LCN= -3.3, water injected from the bottom; (b) LCN= -3.3, water injected from the top.

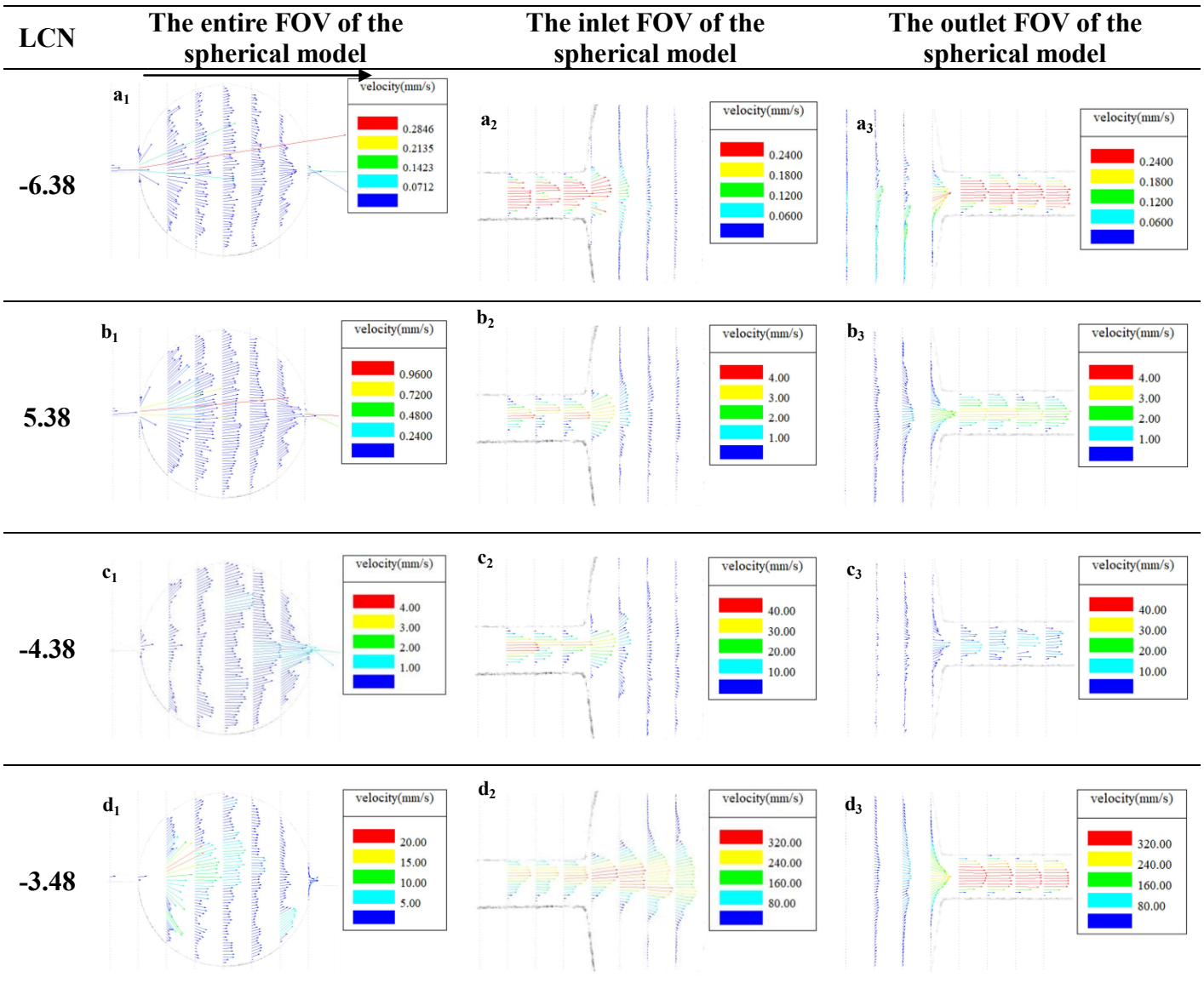

Fig. 23. The oil phase velocity field in the spherical model at different oil injection velocities, where the flow direction is from left to right. a_i-d_i (i=1-3) represent the oil phase velocity field in the spherical model in which LCN is -6.38, -5.38, -4.38, and -3.48, respectively. The lower indices 1, 2, and 3 indicate that the FOV is the entire model, the inlet area, and the outlet area, respectively.

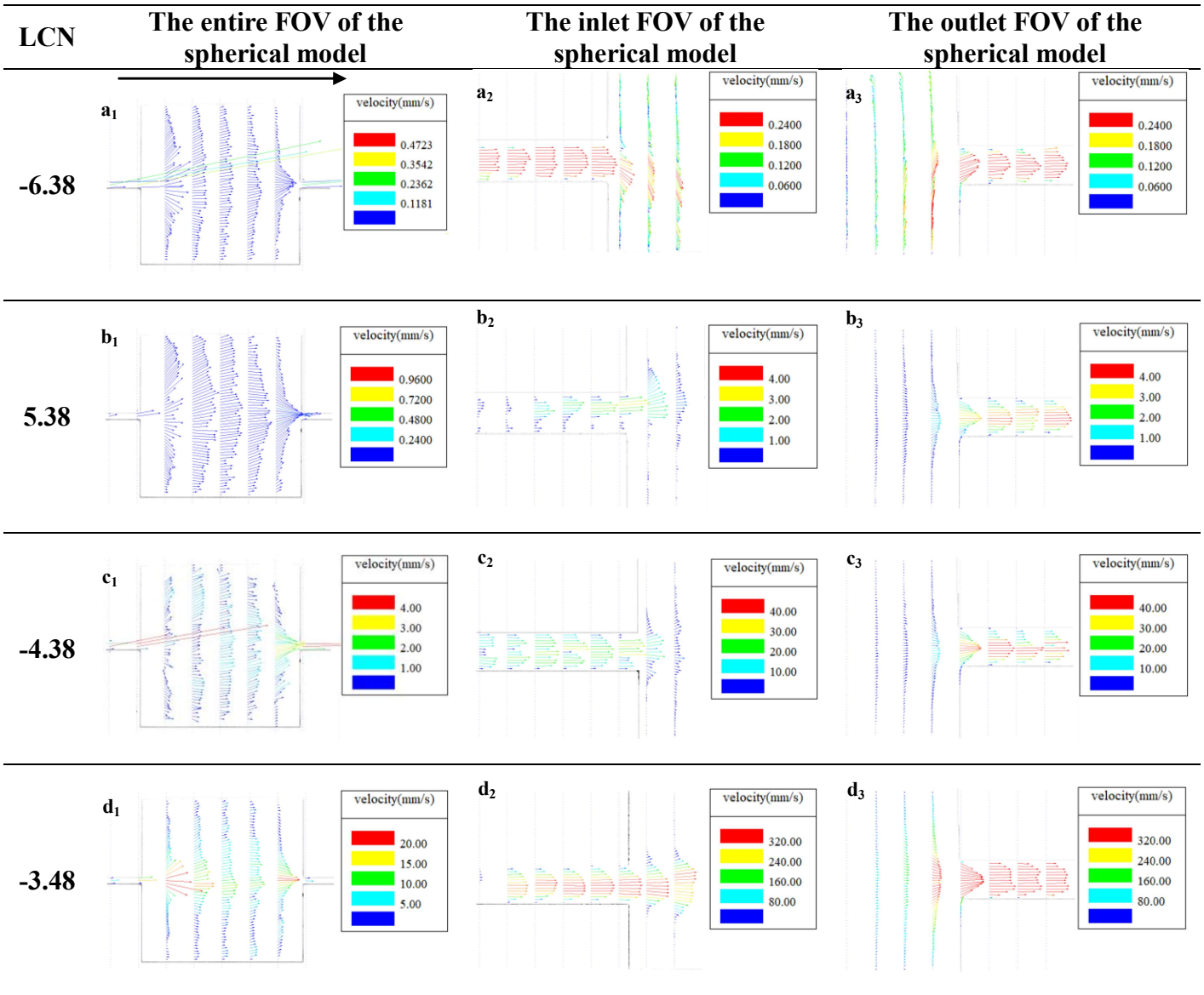

Fig. 24. The oil phase velocity field in the square model at different oil injection velocities, where the flow direction is from left to right. a_i-d_i (i=1-3) represent the oil phase velocity field in the square model in which LCN is -6.38, -5.38, -4.38, and -3.48, respectively. The lower indices 1, 2, and 3 indicate that the FOV is the entire model, the inlet area, and the outlet area, respectively.

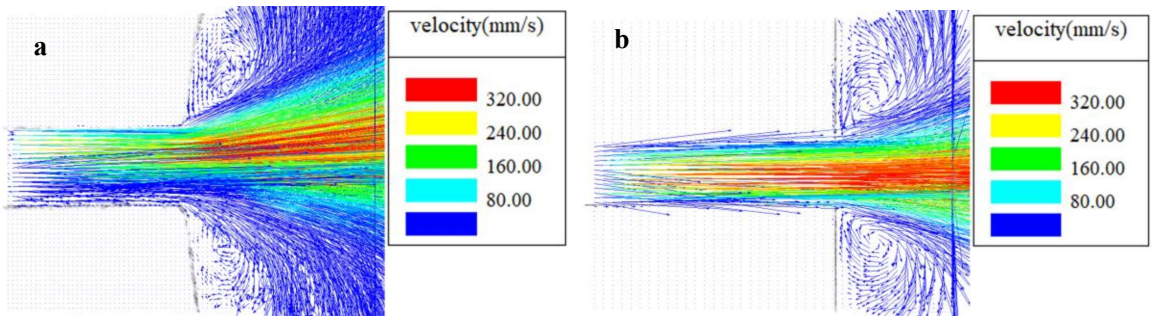

Fig. 25. (a) is the magnification of Fig. 23(e_2); (b) is the magnification of Fig. 24(e_2).

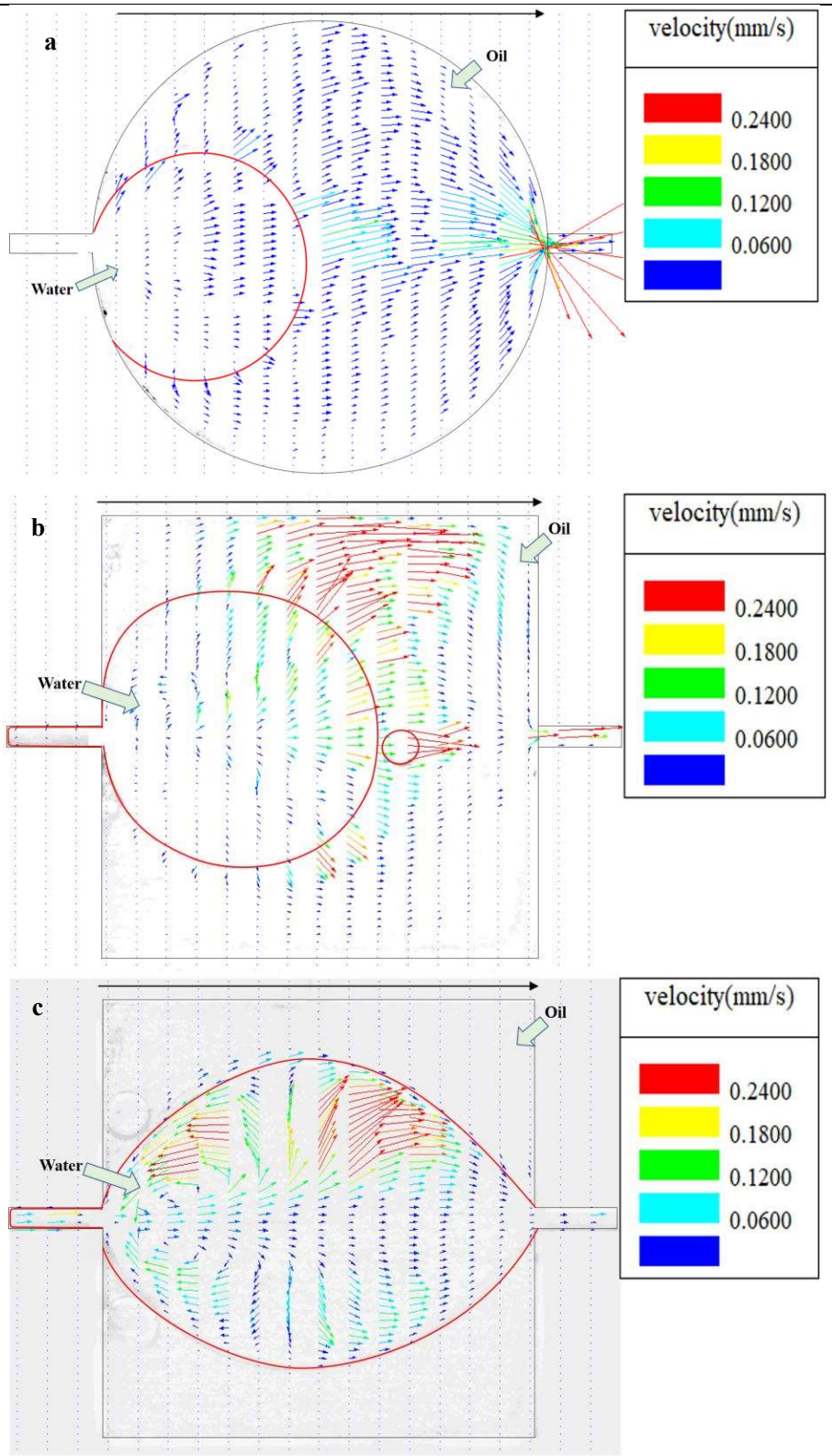

Fig. 26. Horizontal flooding: oil-water velocity field when the LCN is -2.08 in different models, where the flow direction is from left to right and the red line is the oil-water interface. (a) In the spherical model; (b)-(c) In the square model ((b) is the oil-water velocity field during the water injection process, and (c) is the oil-water velocity field when the water is seen at the outlet).

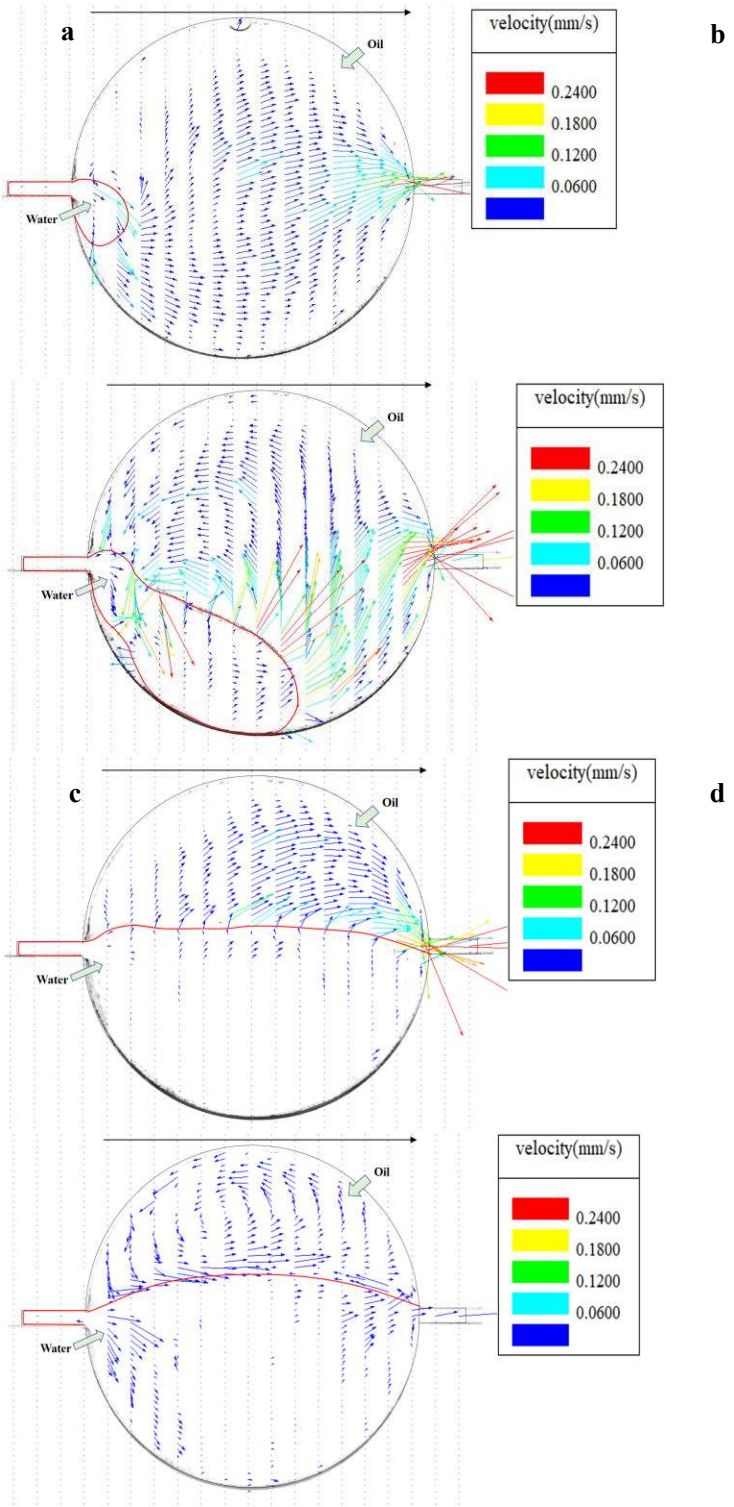
a
Oil
Water
velocity(mm/s)
0.2400
0.1800
0.1200
0.0600
b
Oil
Water
velocity(mm/s)
0.2400
0.1800
0.1200
0.0600
c
Oil
Water
velocity(mm/s)
0.2400
0.1800
0.1200
0.0600
d
Oil
Water
velocity(mm/s)
0.2400
0.1800
0.1200
0.0600

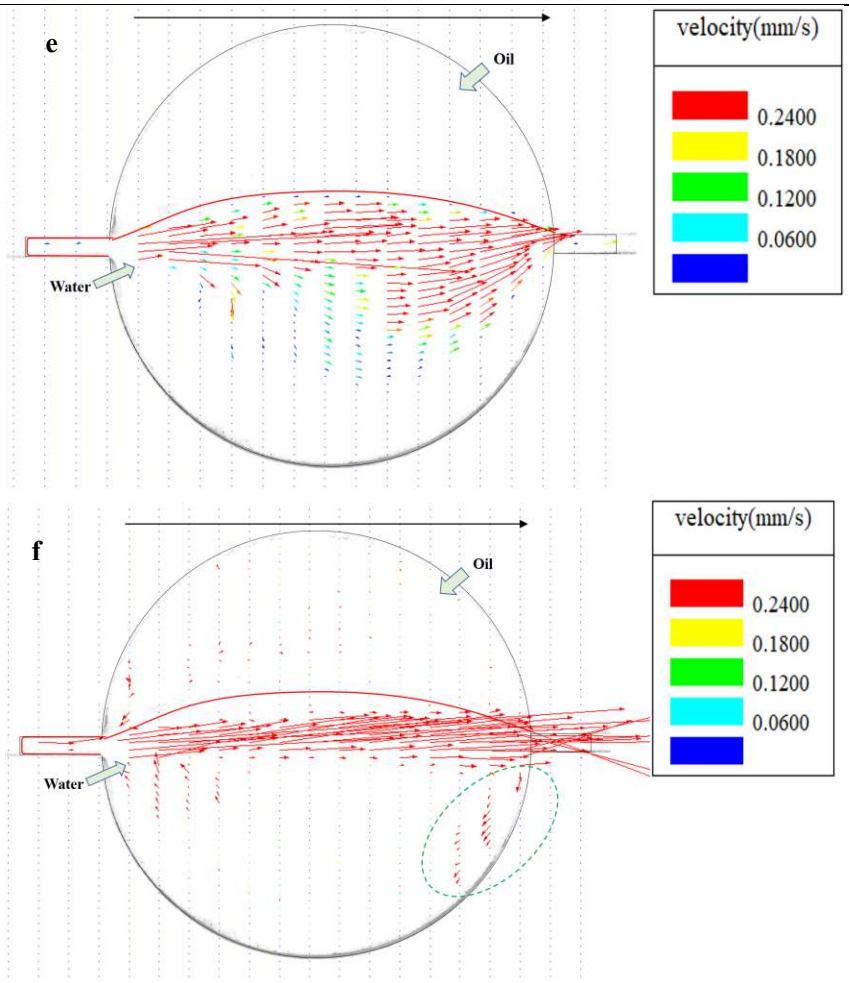

Fig. 27. Vertical flooding: oil-water velocity field at different water injection velocities in the spherical model, where the flow direction is from left to right and the red line is the oil-water interface. (a)-(d): LCN is -3.68 ((a)-(d) are the oil-water velocity field at different water injection times: (a) is when the water just enters the vug; (b) is when the water reaches the bottom of the vug; (c) is when the water flows out of the vug; (d) is when the water is seen at the outlet); (e) LCN=-2.68; (f) LCN=-2.08. The green dotted region shows a reverse water velocity field in the lower horizontal line at the outlet end of the vug.

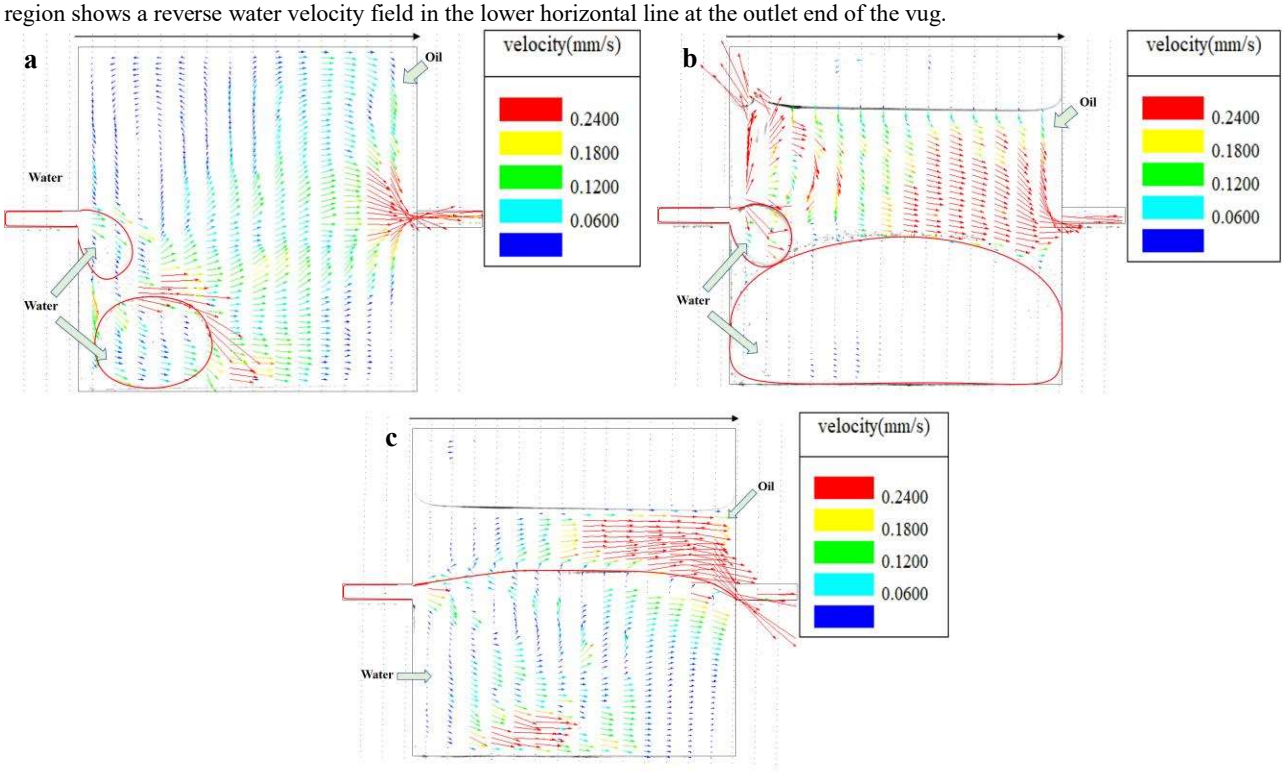

Fig. 28. Vertical flooding: oil-water velocity field at different water injection velocities in the square model, where the flow direction is from left to right and the red line is the oil-water interface. (a)-(c) LCN is -3.68 ((a)-(c) are the oil-water velocity field at different water injection times: (a) is when the water reaches the bottom of the vug; (b) is when the water is about to flow out of the vug; (c) is

when the water is seen at the outlet).

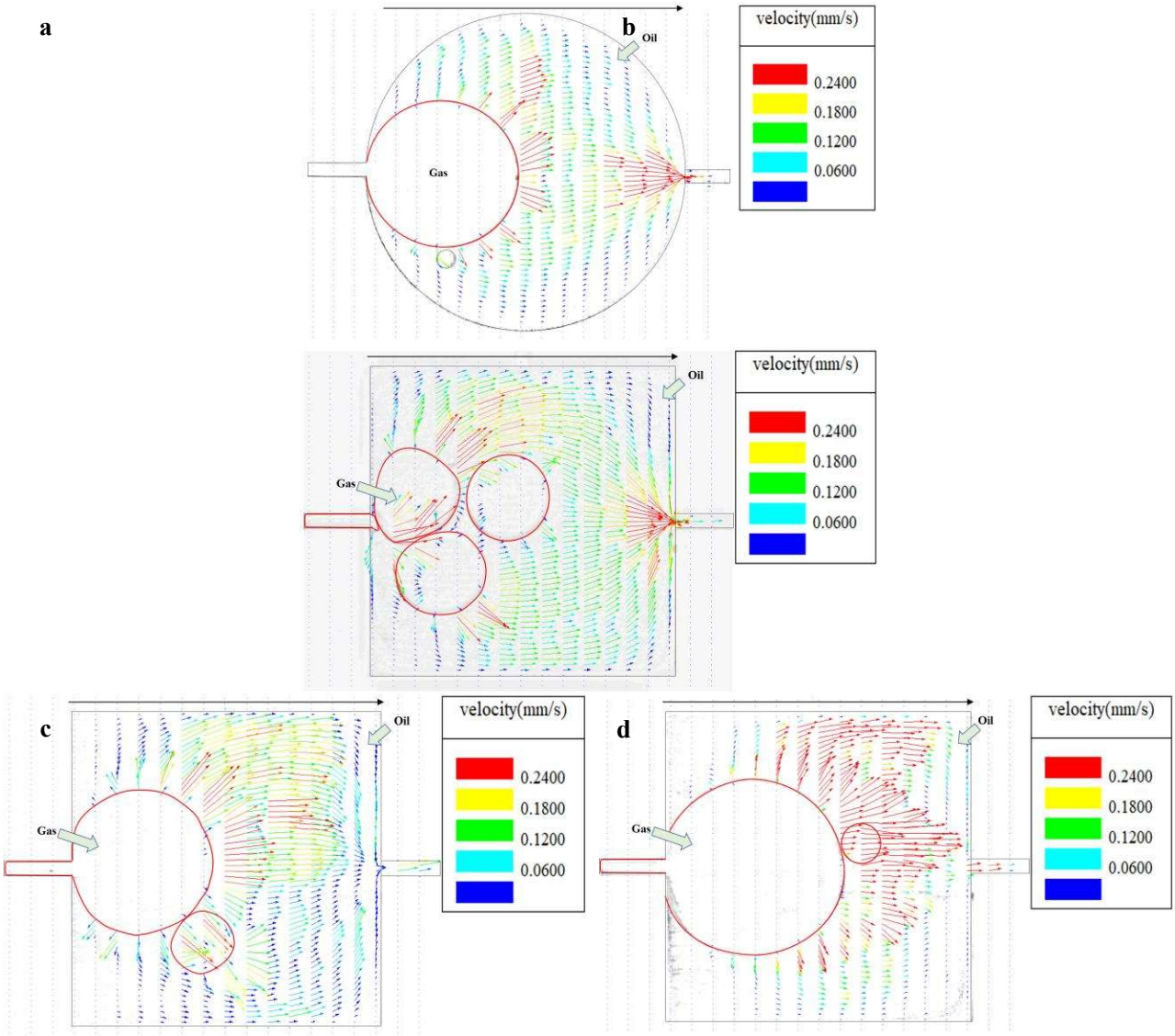

Fig. 29. Horizontal flooding: oil-gas velocity field at different gas injection velocities in different models, where the flow direction is from left to right and the red line is the oil-gas interface. (a) The LCN is -4.38 in the spherical model; (b)-(d) the LCN is -5.38, -4.38, and -3.48 in the square model, respectively.

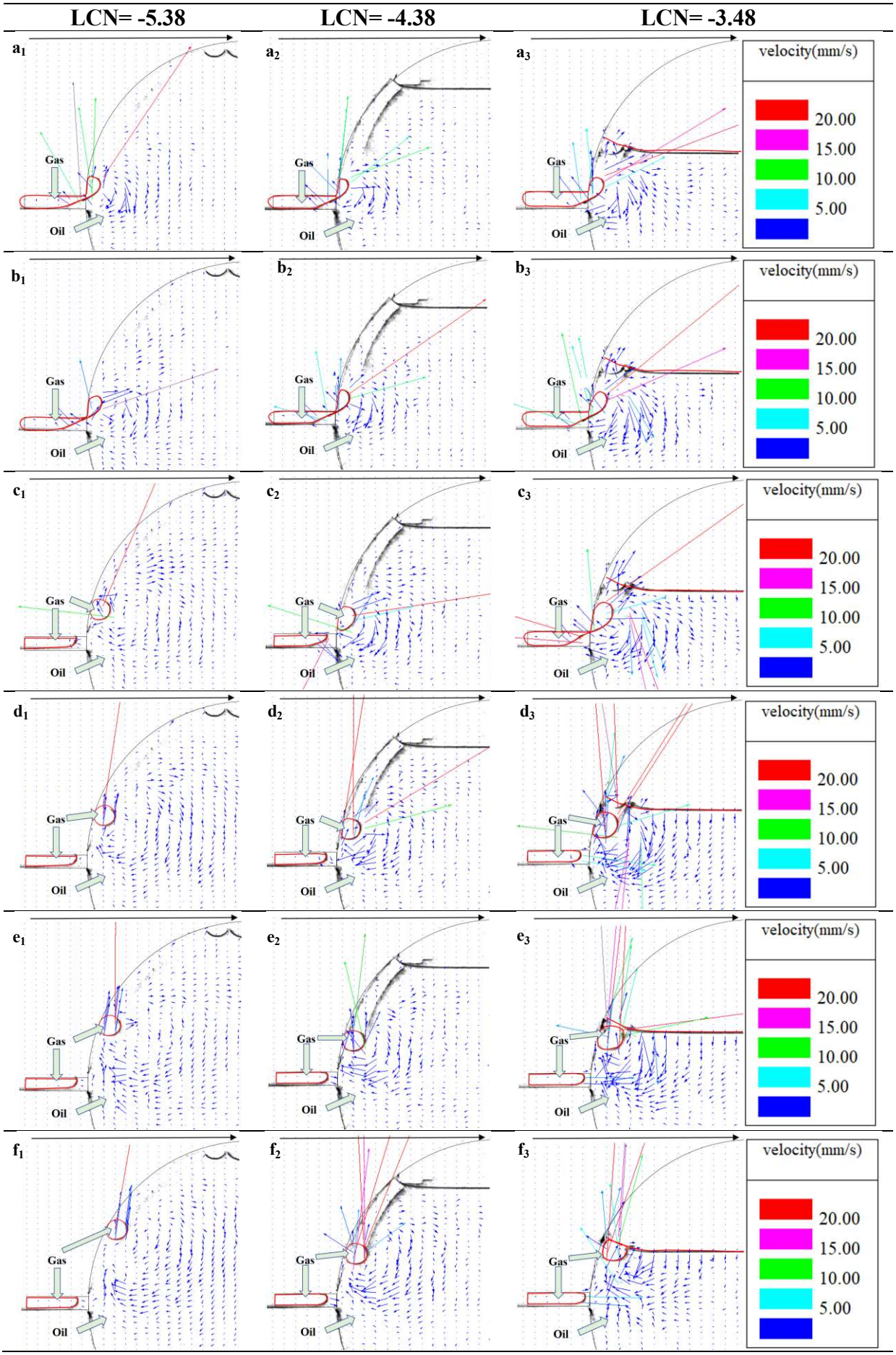

Fig. 30. Vertical flooding: oil-gas velocity field at different gas injection velocities in inlet FOV of the spherical model, where the flow direction is from left to right and the red line is the oil-gas interface. a_i-f_i are the oil-gas velocity field at different gas injection times, respectively. The lower indices 1, 2, and 3 indicate that the LCN is -5.38, -4.38, and -3.48, respectively.